EVALUATION OF PHOTOSTABILITY, CELLULAR UPTAKE, PHOTOCHEMICAL MECHANISM AND PHOTODYNAMIC EFFICACY OF ROSE BENGAL INCORPORATED MESOPOROUS SILICA NANOPARTICLES

by

Tuğçe Mutlu

B.S, in Electrical and Electronics Engineering, İstanbul Bilgi University, 2020

Submitted to the Institute of Biomedical Engineering
in partial fulfillment of the requirements
for the degree of
Master of Science
in
Biomedical Engineering

Boğaziçi University
2024

EVALUATION OF PHOTOSTABILITY, CELLULAR UPTAKE, PHOTOCHEMICAL MECHANISM AND PHOTODYNAMIC EFFICACY OF ROSE BENGAL INCORPORATED MESOPOROUS SILICA NANOPARTICLES

APPROVED BY:

Assist. Prof. Mustafa Kemal Ruhi .....
(Thesis Advisor)

Assist. Prof. Banu İyisan .....

Assist. Prof. Burcu Güleryüz .....

DATE OF APPROVAL: 13 June 2024

ACKNOWLEDGMENTS

I would like to express my deepest gratitude to my advisor, Mustafa Kemal Ruhi, for his continious support, priceless guidance, and unwavering encouragement throughout my research and the writing of this thesis. I would also like to thank my previous advisor, Murat Gülsoy, for his encouragement and teachings during the first semesters of my master's degree. The completion of this job has been made possible by their knowledge and insight.

It has also been a great experience to have my lab friends and colleagues collaborate with me, provide guidance, and brainstorm together. Throughout this journey, they have been a great companion and have made it both productive and enjoyable.

I would like to especially thank my sister, Ece Mutlu, for her constant encouragement and assistance. It has been a great source of strength for me to have your belief in me. I would also like to express my heartfelt appreciation to my entire family for their unconditional love, patience, and support over the years. The faith they have shown in me during my studies has been a crucial part of this thesis' completion.

Also, this study was supported by YÖK-ADP Grant Number 50002. We would like to thank Prof. Dr. Bora Garipcan for their valuable contributions.

ACADEMIC ETHICS AND INTEGRITY STATEMENT

I, Tuğçe Mutlu, hereby certify that I am aware of the Academic Ethics and Integrity Policy issued by the Council of Higher Education (YÖK) and I fully acknowledge all the consequences due to its violation by plagiarism or any other way.

Name :

Signature:

Date:

ABSTRACT

EVALUATION OF PHOTOSTABILITY, CELLULAR UPTAKE, PHOTOCHEMICAL MECHANISM AND PHOTODYNAMIC EFFICACY OF ROSE BENGAL INCORPORATED MESOPOROUS SILICA NANOPARTICLES

Cancer is a complex disease that poses a significant global threat to human health. Traditional treatment methods, may not be effective in all cases and often result in numerous side effects. Photodynamic therapy (PDT) utilizes photosensitizing agents and light of specific wavelengths to selectively kill malignant cells without harm other tissue. However, the photosensitizing agents used in PDT often face challenges such as poor solubility in blood or low lipophilicity, which causes aggregation or inefficient accumulation of these agents in tumor tissue. To address these issues, drug delivery systems like mesoporous silica nanoparticles (MSNs) are employed to deliver the photosensitizing agents to the tumor site efficiently. In this study, Rose Bengal, a photosensitive compound, was incorporated with MSNs and tested on the A-549 lung cancer cell line in terms of photostability, cellular uptake, photochemical mechanism, and photodynamic efficacy. The results showed that Rose Bengal-incorporated MSNs produced more singlet oxygen compared to free Rose Bengal. Additionally, the photostability of Rose Bengal was enhanced when incorporated into the mesoporous silica matrix. The cellular uptake did not show a significant change. However, it should be kept in mind that these experiments were conducted on an *in vitro* model and the real effect of this drug delivery strategy would be revealed in *in vivo* conditions, where circulation and extravasation take place. Future research will focus on investigating the efficacy of this method on *in vivo* models and modifying the nanoparticles to further enhance the efficacy of the proposed treatment accordingly.

Keywords: Cancer, Photodynamic Therapy, Mesoporous Silica Nanoparticles, Rose Bengal

ÖZET

ROSE BENGAL YÜKLÜ MEZOGÖZENEKLİ SİLİKA NANOPARTİKÜLLERİNİN FOTOSTABİLİTESİ, HÜCRESEL ALIMI, FOTOKİMYASAL MEKANİZMASI VE FOTODİNAMİK ETKİNLİĞİNİN DEĞERLENDİRİLMESİ

Kanser, dünya çapında insan sağlığına yönelik önemli bir tehdit oluşturan karmaşık bir hastalıktır. Kemoterapi ve radyoterapi gibi geleneksel tedavi yöntemleri her durumda etkili olmayabilir ve çok sayıda yan etkiye neden olabilir. Fotodinamik terapi (FDT), çevredeki sağlıklı dokuya verilen zararı en aza indirirken malin hücreleri seçici olarak yok etmek için ışığa duyarlı ajanlar ve belirli dalga boylarında ışığı kullanır. Ancak, ışığa duyarlı ajanların kanda çözünmemesi veya düşük lipofiliklik gibi özellikleri nedeniyle agragasyon veya tümör dokusunda toplanamama gibi FDT etkinliğini düşüren sorunlara neden olabilir. Bu sorunları çözmek ve ışığa duyarlı ajanları tümör bölgesine verimli bir şekilde iletmek için mezogözenekli silika nanoparçacık (MSNs) gibi ilaç taşıyıcı sistemleri kullanılır. Bu çalışmada, ışığa duyarlı bir bileşik olan rose bengal, MSNs ile birleştirildi ve A-549 akciğer kanseri hücre hattı üzerinde fotostabilite, hücresel alım, fotokimyasal mekanizma ve fotodinamik etkinlik açısından test edildi. Sonuçlar, rose bengal yüklü MSNs'lerin, serbest rose bengal ile karşılaştırıldığında daha fazla tekil oksijen ürettiğini gösterdi. Ek olarak, mezogözenekli silika matrisine yüklendiğinde rose bengalin fotostabilitesinin arttığı görüldü. Hücre içine alım açısından istatistiksel olarak anlamlı bir farklılık gözlenmese de bu deneylerin *in vitro* model üzerinde yapıldığı ve bu stratejinin gerçek etkisinin dolaşımın ve ekstravazasyonun gerçekleştiği *in vivo* koşullarda ortaya çıkacağı unutulmamalıdır. Gelecekteki araştırmalar, bu yöntemin *in vivo* modeller üzerindeki etkinliğini araştırmaya ve alınacak sonuçlara göre önerilen tedavinin etkinliğini daha da artırmak için nanoparçacıkların yapısında değişiklik yapmaya odaklanacaktır.

Anahtar Sözcükler: Kanser, Fotodinamik Terapi, Mezogözenekli Silika Nanopartikülleri, Rose Bengal

TABLE OF CONTENTS

LIST OF FIGURES

LIST OF TABLES

LIST OF SYMBOLS

$^1O_2$	Singlet Oxygen
mW/cm^2	Milliwatts per Square Centimeter
J/cm^2	Joules per Centimeter Square
µg/mL	Microgram per Milliliter
O_2	Oxygen
CO_2	Carbon Dioxide
mM	Millimolar
mL	Milliliter
nm	Nanometer
M_{rb}	Molar Weight of Rose bengal

LIST OF ABBREVIATIONS

ANOVA	Analysis of Variance
APTES	(3-Aminopropyl)triethoxysilane
CTAB	Cetyltrimethyl Ammonium Bromide
DI Water	Distilled Water
DLS	Dynamic Light Scattering
DMEM	Dulbecco's Modified Eagle Medium
DMSO	Dimethyl Sulfoxide
DNA	Deoxyribonucleic Acid
DPBF	1,3-Diphenylisobenzofuran
EPR	Enhanced Permeability and Retention
FBS	Fetal Bovine Serum
LED	Light Emitting Diode
MPR	Microplate Reader
MSN	Mesoporous Silica Nanoparticle
MTT	3-(4,5-Dimethylthiazol-2-yl)-2,5-Diphenyltetrazolium Bromide
NSCLC	Non-Small Cell Lung Cancer
PBS	Phosphate Buffered Saline
PDT	Photodynamic Therapy
PS	Photosensitizer
RB	Rose Bengal
RB-MSN	Rose Bengal Incorporated Mesoporous Silica Nanoparticle
ROS	Reactive Oxygen Species
SCLC	Small Cell Lung Cancer
SEM	Scanning Electron Microscope
TEOS	Tetraethyl Orthosilicate
UV-Vis	UV-Visible Spectroscopy

1. INTRODUCTION

Cancer remains a life-threatening disease. Current treatments, including chemo therapy, radiation, and surgery, often have serious side effects that significantly impact patients' quality of life. The outcomes of these treatments highlight the need for ongoing efforts to discover more effective methods with low side effects for various types of cancer.

Lung cancer is one of the deathliest cancer type in men and woman. In 2012, lung cancer was responsible for 1.6 million deaths globally [1]. Its insidious nature often results in late-stage diagnoses, which diminishes the effectiveness of therapeutic interventions [2]. Despite recent advancements, the aggressive nature of lung cancer necessitates continuous research and the development of innovative, targeted treatments.

PTD has became commonly studied cancer treatment method. PDT induces a series of reactions that create toxicity in targeted cells, leading to their destruction. In this process, a photosensitizing molecule (photosensitizer) is excited by light at a specific wavelength, which leads to the production of reactive oxygen species (ROS) that mediate cell death [3]. PDT is advantageous over other treatment approaches because it allows for specific and targeted treatment based on light administration. Since the photosensitizing agent becomes toxic only under light exposure, PDT minimizes side effects and reduces damage to surrounding tissues. Additionally, PDT can be used in a combination with other treatment methods [4]. Despite promising features, PDT has also limitations. For example, photosensitizer molecules used in PDT often face challenges such as poor solubility in blood and inefficient accumulation in tumor tissue. Liposomes and nanoparticles and other drug delivery methods may provide better stability and longer circulation time [5]. An important phenomenon that leads to the accumulation of molecules in tumor is Enhanced-Permeability and Retention (EPR) Effect. Due to EPR, nanoparticles of size between 1 and 100 nanometers can accumulate in tumors [6],[7].

This study focuses on using a nanoparticle called mesoporous silica to deliver Rose Bengal (RB) to the target site. RB is a photosensitizer that has an absorption peak in the green region of visible light spectrum. In addition to its high $^1O_2$ production, RB is known as its low dark toxicity [8]. Although RB has advantages, its effectiveness is limited due to poor cellular uptake [9]. In this study, we aimed to use Mesoporous silica nanoparticles (MSNs) as a delivery system to increase the efficacy of RB and the final nanoparticles were tested in *in vitro* studies.

1.1 Motivation and objectives

Lung cancer is one of the leading types of aggressive diseases that threaten human life. Despite efforts to prevent the disease with treatments such as chemotherapy and radiotherapy, these methods may not be successful, particularly when the disease is diagnosed at advanced stages. Furthermore, the side effects of the treatments have a significant impact on both the patient's health and psychologically. Therefore, studies continue to develop novel treatments.

As an alternative, PDT offers a selective and minimally invasive treatment with low side effects than chemotherapy and radiotherapy. PDT is selective because the photosensitizer becomes toxic only when it is excited by light directed to the target area [10],[11]. Furthermore, the utilization of nanoparticles can enhance the delivery of photosensitizers to tumors [12].

This study aims to improve the efficacy of RB-mediated PDT by using MSNs. Our investigation was divided into three steps to evaluate the therapeutic potential of RB-MSNs on the A-549 lung cancer cell line: synthesis, treatment, and analysis. In the synthesis step, MSNs were synthesized and RB molecules were incorporated with nanoparticles. The morphology and size of the generated MSNs were investigated using the Scanning Electron Microscope (SEM) and Dynamic Light Scattering (DLS). A standard curve was used to calculate the amount of RB incorporated into MSNs. In the treatment step, the toxicity of RB in the dark was assessed to determine the

highest non-toxic dose of RB-incorporated MSNs. The amount of RB in RB-MSNs was calculated using the standard curve. PDT was then conducted using RB-MSN nanoparticles. In the last step, The stability and cellular uptake of RB-MSNs, as well as the photochemical mechanism of the method were analyzed.

1.2 Organization of thesis

Chapter 1, provides a comprehensive explanation of the concept of the study, identifies motivation and specific aims of the research. Chapter 2 explains the research within the current literature and emphasizes its significance. Chapter 3 includes thorough explanations and visual aids that describe the materials and methodology utilized. Chapter 4 reveals the results of the experiments. Chapter 5 critically examines and interprets the results in the context of existing literature. Chapter 6 presents the outcome of the study along with a summary of the results and offers suggestions for future work and improvements.

2. BACKGROUND

2.1 Lung cancer: Global impact and prevention efforts

According to statistics, lung cancer is one of the most often diagnosed forms of cancer worldwide, accounting for 11.4 of all cancer cases [13]. The research conducted in 2020 shows us that 2.21 million new lung cancer patients were detected worldwide, and 1.8 million people lost their lives due to this disease [14]. The incidence of lung cancer and related mortality varies by country, based on factors such as ease of access to health care and, most significantly, smoking rates [15]. Although smoking is the main contributory factor of lung cancer, non-smokers may suffer from the disease due to cigarette smoke exposure, genetic predisposition, and pollutant exposure. The two types of lung cancer is small-cell lung cancer (SCLC) and non-small-cell lung cancer (NSCLC), which differ in their morphological structure under a microscope and aggressive activity within the body [16]. Squamous cell carcinoma evolves because of structural damage in the lungs as an effect of smoking and is often seen in cells in the respiratory tract. Large cell carcinoma is expressed as the rarest but most aggressive and rapidly developing type of lung cancer among the NSCLC types [17]. Although the incidence of SLCL is lower compared to instances of NSCLC, it is quite dangerous due to its rapid growth and tendency to metastasize even in the early stages. The majority of SCLC cases are directly linked to smoking [18]. All these forms of lung cancer pose serious risks to the lives of individuals and continue to be a major burden on the worldâs medical systems. With ongoing research into cancer treatment from the past to the present, new treatment methods and breakthroughs have substantially improved disease prevention, particularly in early detection. Historically, medical professionals used surgical removal to treat cancer. However, the increased risk of cancer recurrence with this treatment has motivated experts to investigate alternative preventative therapies. As time passed, near the end of the twentieth century, surgical operations were supported by newly found chemotherapy treatments. Their effectiveness was considerably boosted over time by new medications [19]. Nowadays, research

is being conducted to lessen the negative effects of existing therapeutics, improve the effectiveness of combined treatments, and take efficiency to the next level by utilizing nanoparticles.

2.2 Photodynamic therapy: Innovations in cancer treatment

Considering its benefits including minimal invasiveness, targeted action, and reduced side effects, PDT is gaining attention for cancer treatment. In PDT process illustrated in Figure 2.1, light-sensitive chemicals accumulate in the cancerous area and become toxic through a series of reactions when exposed to light [20],[21]. The photosensitive chemical, which becomes toxic when light is applied to the target location, enables for more localized treatment while minimizing damage to surrounding healthy tissue [22]. PDT can be repeatedly applied and used in combination with other treatment techniques [23],[24]. Furthermore, it helps to maintain the patients' high standard of living during the period of treatment as the duration of the treatment is typically short [25]. PDT creates diverse reactions based on the type of photosensitive chemical used, and the level of toxicity varies depending on the type of oxygen produced. Two types of reactions occur: type 1-type 2 reactions. In type 1 reactions, PS is excited to a singlet excited state. PS molecules returning to the ground state transmit their energy to nearby molecules, leading to electron transfer and producing radicals [26],[27]. In type 2 reactions, the PS molecules that return to the ground state transfers energy to oxygen molecules to excite them to singlet state, which is toxic for cells [28].

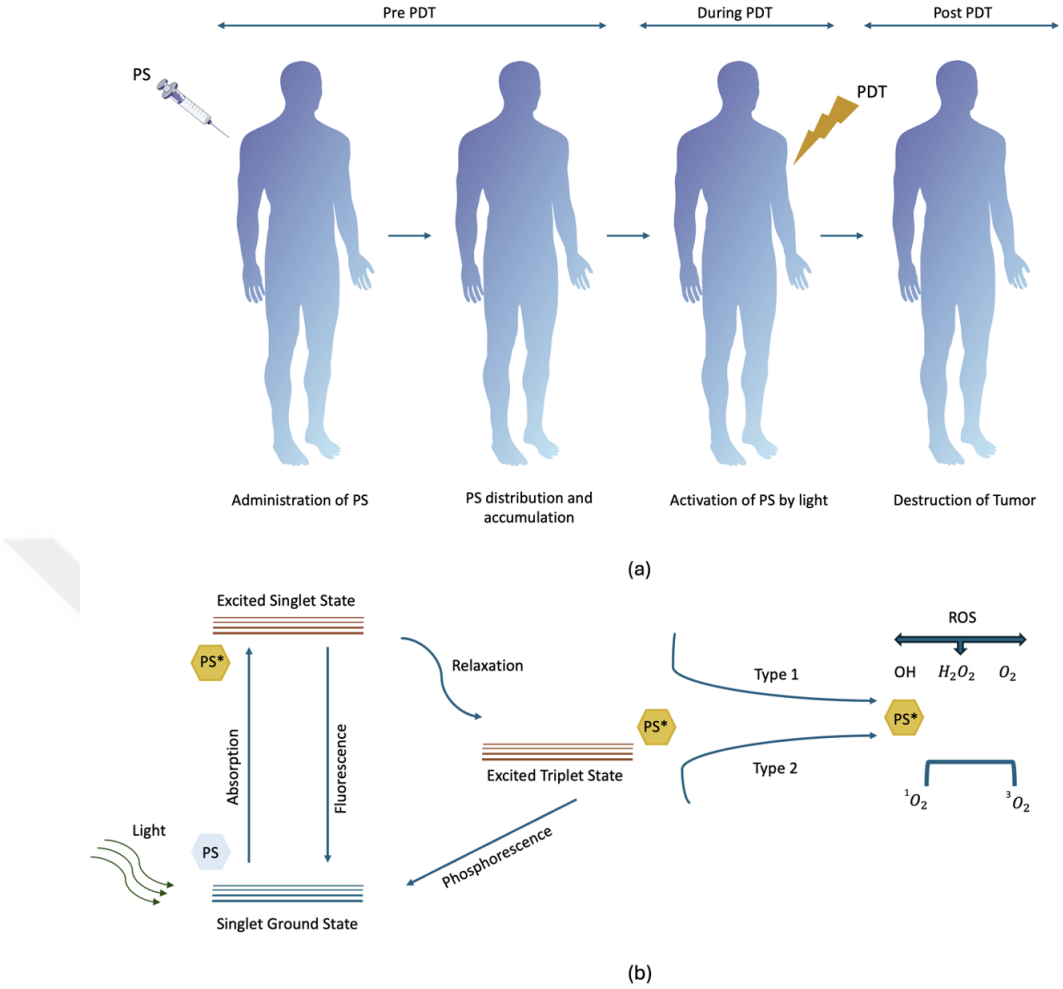

Figure 2.1 (a) Mechanism of PDT, showing activation of the PS by light and ROS generation. (b) Photochemical reactions during PDT including Type I (radicals and ions) and Type II $^1O_2$ processes.

2.3 Nanoparticle-based drug delivery for cancer treatment

In recent decades, it is becoming increasingly prevalent to use delivery methods based on nanoparticles to bring drugs to the desired location [29]. The widespread use of nanoparticle-based delivery systems provides significant benefits in terms of increasing therapeutic efficacy and, in many cases, minimizing patient discomfort due to side effects [30]. The combined use of the drugs with the appropriate nanoparticle can ensure targeting to the tumor site, reducing leakage onto healthy cells and increasing the concentration of drug accumulated in the cancer area [31],[32]. Furthermore, carrier nanostructures prevent drugs from being rapidly eliminated by the body's circulatory system and can help preserve their structural integrity [33].

Among the nanoparticles used for drug delivery systems, liposomes, found by Alec D. Bangham, are the most widespread. They enable the encapsulation of both hydrophilic and hydrophobic medicines, reducing leakage and side effects while allowing for regulated drug release [34]. Polymeric nanoparticles, discovered at the end of the twentieth century and used extensively since that time, give hope for cancer treatments by enhancing the drug's solubility and stability while also making it more functional in terms of targeting ability [35]. Donald Tomalia created dendrimers, which resemble a branched tree, in the late 1970s. Because of their highly modifiable structure, dendrimers have yielded very beneficial results in drug administration, including high drug storage and imaging [36]. In addition to these nanoparticles, micelles discovered in the early twentieth century have shown remarkable results in the dissolution of hydrophobic drugs due to their amphiphilic structure, and inorganic nanoparticles have shown impressive outcomes in cancer treatment through photothermal procedures, imaging, and magnetic investigation [37],[38]. Aside from these examples, many other polymeric nanoparticles have been found in recent years, like carbon-based nanoparticles, quantum dots, and silica nanoparticles for drug delivery [39].

2.3.1 Mesoporous silica nanoparticles

Mesoporous silica nanoparticles (MSN) are easy to synthesize and advantageous for drug loading due to their high surface area and biocompatibility [40]. Additionally, these nanoparticles are optically transparent, which is ideal for light-based applications. Furthermore, it has been shown that incorporation with MSN may increase the $^1O_2$ quantum yield of PSs [41],[42]. There are studies in the literature that considered MSN as a delivery vehicle for RB. In a theoretical study by Estevao *et al.* demonstrated that RB-incorporated MSNs can increase $^1O_2$ production efficiency by preventing aggregation [43]. According to another study of the same research group, the optimized nanoconjugate, 4% RB-incorporated MSNs reduced cell proliferation of melanoma cells (SK-MEL-28) [44]. Additionally, the authors showed that MSNs provide protection against photodegradation by creating a shielding effect for RB. Zhan *et al.* functionalized pH-responsive MSNs with Fe3O4 and utilized them for RB delivery

[45]. The analyses on the cellular uptake, drug release and concentration-dependent apoptosis rates on B16 mouse melanoma cells showed that the treatment with the developed nanoconjugates provided higher rates of apoptosis on B16 cells compared to free RB with minimal dark toxicity. Despite these and other efforts, to the authors knowledge, there is no comprehensive study in the literature that evaluates RB-incorporated MSNs (RB-MSNs) in terms of photostability, cellular uptake, photochemical mechanism, and PDT efficacy. Our research aims to fill this gap by investigating the efficiency of RB-incorporated MSNs as a PDT agent on the A-549 lung cancer cell line.

3. MATERIALS and METHODS

3.1 Synthesis of nanoparticles

Ammonium-hydroxide (NH_4OH), cetyltrimethylammonium-bromide (CTAB), hydrochloric-acid (HCl), tetraethyl-orthosilicate (TEOS), (3-Aminopropyl) triethoxysilane (APTES), RB and ethanol were obtained from Sigma-Aldrich.

The synthesis of RB incorporated MSNs nanoparticles stated in the study begins with the synthesis of MSNs nanoparticles. Afterwards, (3-Aminopropyl) triethoxysilane (APTES) modification was conducted to improve the loading rate of RB nanoparticles into the MSNs pores. Finally, powdered RB is mixed with MSNs using a magnetic stirrer to integrate RB with MSNs (Figure 3.1).

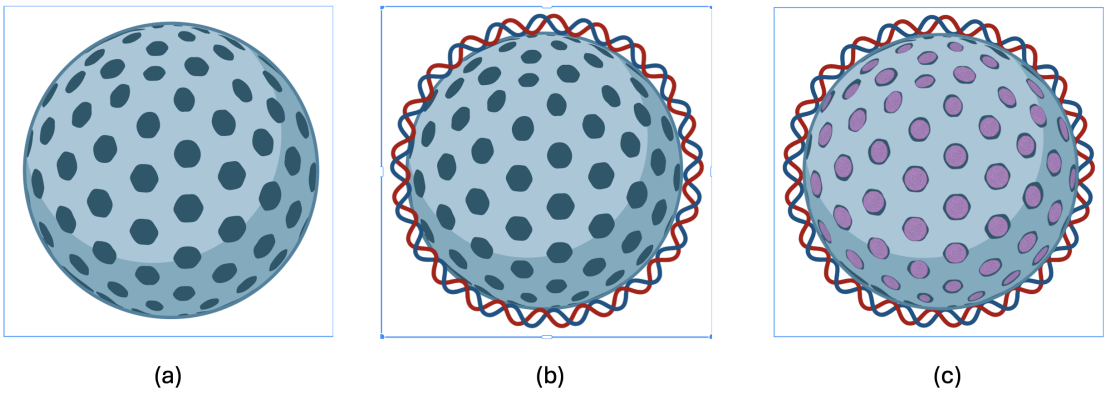

Figure 3.1 (a) MSN (b) MSN functionalization with APTES (c) RB-MSN.

Table 3.1
Chemicals utilized for MSNs preparation.

Chemical Substances	Quantity Utilized	Molecular Weight (g/mol)
NH_4OH	1.057 mL	71.09
CTAB	0.058 g	364.62
TEOS	118 µL	208.37
HCL	2o µL	36.46
APTES	12 µL	145.33
RB	3 mg	1019.62

3.1.1 Synthesis of mesoporous silica

MSNs were synthesized as described previously [46]. Briefly, 7.5 mL of distilled water and 1.057 mL of NH_4OH were mixed using a magnetic stirrer. The mixture was then completed to 30 mL by adding 21.44 mL of distilled water, and mixed again at 500 rpm and 40°C. Subsequently, 0.058 g CTAB was added into the mixture and allowed to dissolve. 118 µL TEOS and 482 µL ethanol were gradually added to the mixture, the temperature was raised to 60°C, and the mixture was stirred for two hours in order to precipitate the nanoparticles. After 2 hours, the nanoparticle solution was washed three times with ethanol using a centrifuge and a sonicator. For the washing process, the synthesized mesoporous silica nanoparticles were transferred to centrifuge tubes and centrifuged at 14800 rpm for 15 minutes. After centrifugation, the supernatant was carefully discarded and fresh ethanol was added to the vials. The mixture was then sonicated to ensure a homogeneous suspension. This washing step was repeated two more times to completely remove any remaining surfactant and unreacted materials. The precipitated nanoparticles were dissolved in 20 mL ethanol, and 20 µL HCL was added. The mixture was then stirred at 500 rpm and 60°C for 3 hours. Finally, the MSNs were washed three times with ethanol.

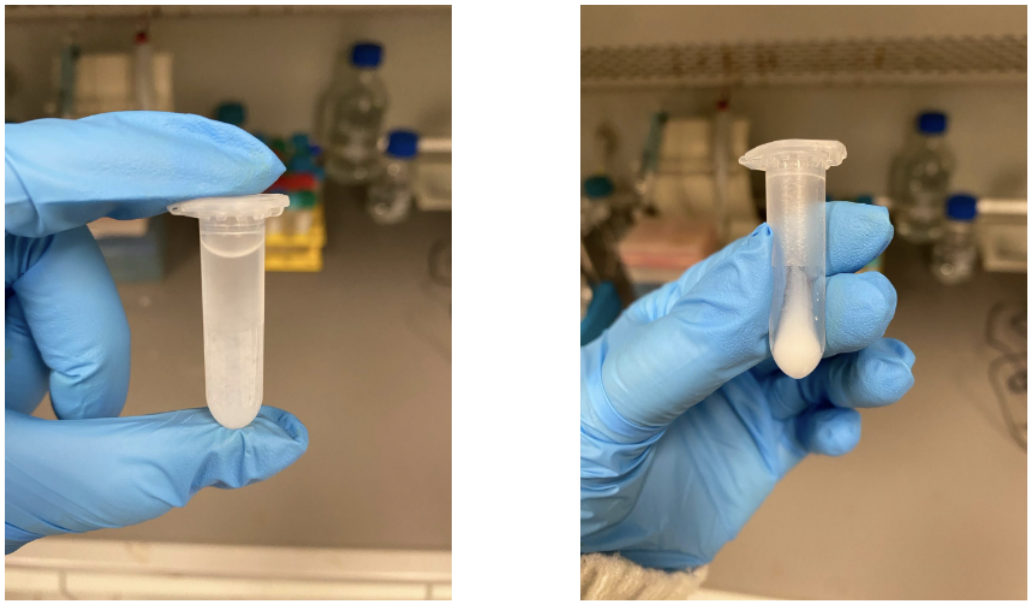

Figure 3.2 MSNs (a) before (b) after washing steps.

3.1.2 Amino-functionalization of mesoporous silica using APTES

APTES is a chemical widely utilized in biology and chemistry, particularly for the surface modification and functionalization of silica-based nanoparticles like MSNs [47]. When APTES is added to the MSN solution, it forms a covalent bond with the (-Si-OH) silanol groups on the silica surface, resulting in amino groups covering the MSNs surface. This surface modification method improves the nanoparticles stability, as well as prevents aggregation of incorporated molecules in MSN pores, ensuring uniform dispersion [48]. In our study, MSNs were dissolved in 15 mL of ethanol, and 12 µL of APTES was slowly added on MSNs. The mixture was stirred in the magnetic stirrer at 500 rpm at room temperature for 24 hours. The mixture was then washed three times with ethanol.

3.1.3 Incorporation of RB into MSNs

APTES-functionalized MSNs were dissolved in 15 mL of ethanol and mixed with 3 mg of RB. The mixture was stirred at 500 rpm and room temperature for 24 hours. The synthesized nanoparticles were then washed three times with ethanol, dissolved in distilled water, and kept in the freezer for use in future experiments.

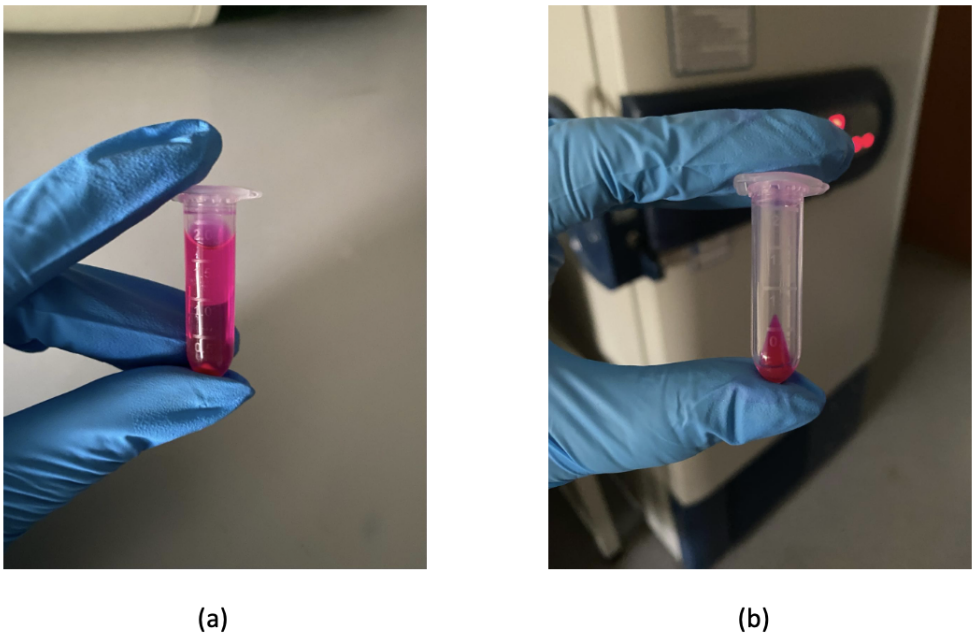

Figure 3.3 RB incorporated MSNs (a) before (b) after washing steps.

3.2 Characterization of nanoparticles

A standard curve was generated using the absorbance values of 20-200 µg/mL RB at 570 nm using the UV-VIS spectrophotometer to determine the RB amount in synthesized RB-MSNs. The absorption-spectra of the nanoparticles were obtained using a Nanodrop 2000c UV-VIS spectrophotometer. A Scanning Electron Microscope (SEM) was utilized to determine the morphology of synthesized nanoparticles. Before imaging the nanoparticles, approximately 15 mg of MSNs were dissolved in 1.5 mL ethanol and a homogeneous distribution was obtained using a sonicator. Subsequently, a drop of dissolved MSN was placed on the SEM templates, and images were taken. Dynamic light scattering (DLS) technique was used to determine the size distribution, which relies on examining the light intensities caused by the movement and collision of molecules, known as Brownian motion [49]. Before DLS analysis, the synthesized MSNs were kept in a 60°C oven for 24 hours and the number of synthesized MSNs was quantified using a precision weighing instrument. Approximately 15 mg of synthesized MSNs were dissolved with 1.5 mL ethanol, and the content was sonicated for homogenization and to prevent aggregation before DLS analysis.

3.3 Cell culturing and dark toxicity experiments

The A-549 lung cancer cells were cultured in conditions recommended by the manufacturer. Adherent cells were cultured using DMEM medium supplemented with 10% FBS and 1% penicillin/streptomycin solution. The cells were maintained at 37°C and 5% CO_2. The medium was refreshed regularly until the until the A-549 cell line achieved 80% - 90% confluency and detached from the flasks using Trypsin-EDTA for seeding or passaging.

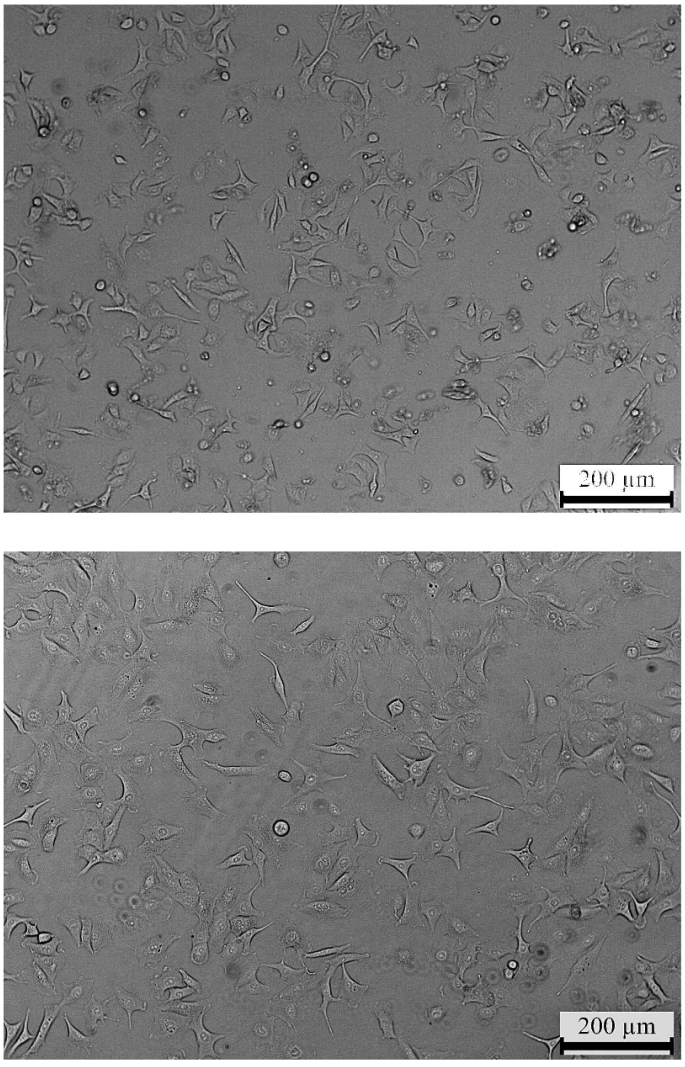

Figure 3.4 Representative images of A-549 lung cancer cells around 70% confluency under a bright-field microscope with 10x magnification. Scale bar: 200 µm

3.3.1 Cell plating in different experiments

Toxicity experiments were performed by seeding cells (1×10^4) into 96-well plates. In dark toxicity experiments, a total of 60 wells were seeded for a control and 9 different application groups. Each group consists of 6 technical replicates, as seen in Figure 3.5(a). For PDT experiments, a total of 24 wells were seeded for 6 different groups, including a no-treatment control. Each group consists of 4 technical replicates as seen in Figure 3.5(b). To investigate the role of $^1O_2$ in cellular toxicity, firstly, the toxicity of two control groups and two different concentrations of sodium azide on the cells were examined, as seen in Figure 3.6(a). The non-toxic value found subsequently was compared with the most effective PDT parameters, as seen in Figure 3.6(b). For the uptake experiment, 1.5×10^5 cells were seeded as shown in Figure 3.7. The seeded cells were incubated for 1 day at 5% CO_2 and 37°C for 24 hours.

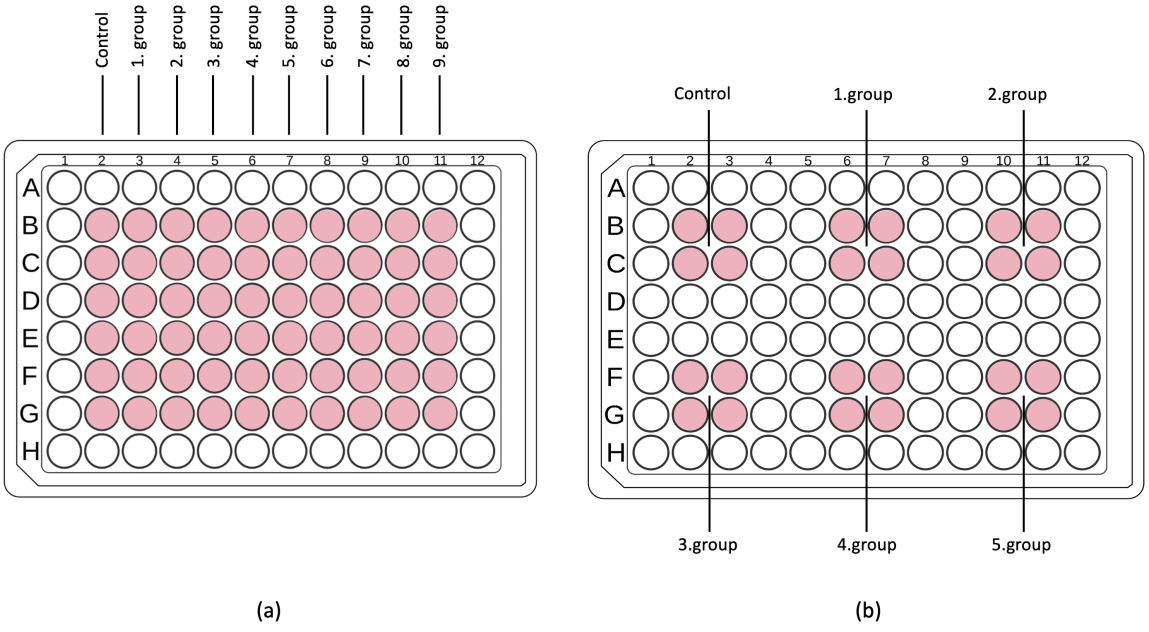

Figure 3.5 Illustration of the 96-well plate seeding layout for (a) dark toxicity (b) PDT experiments.

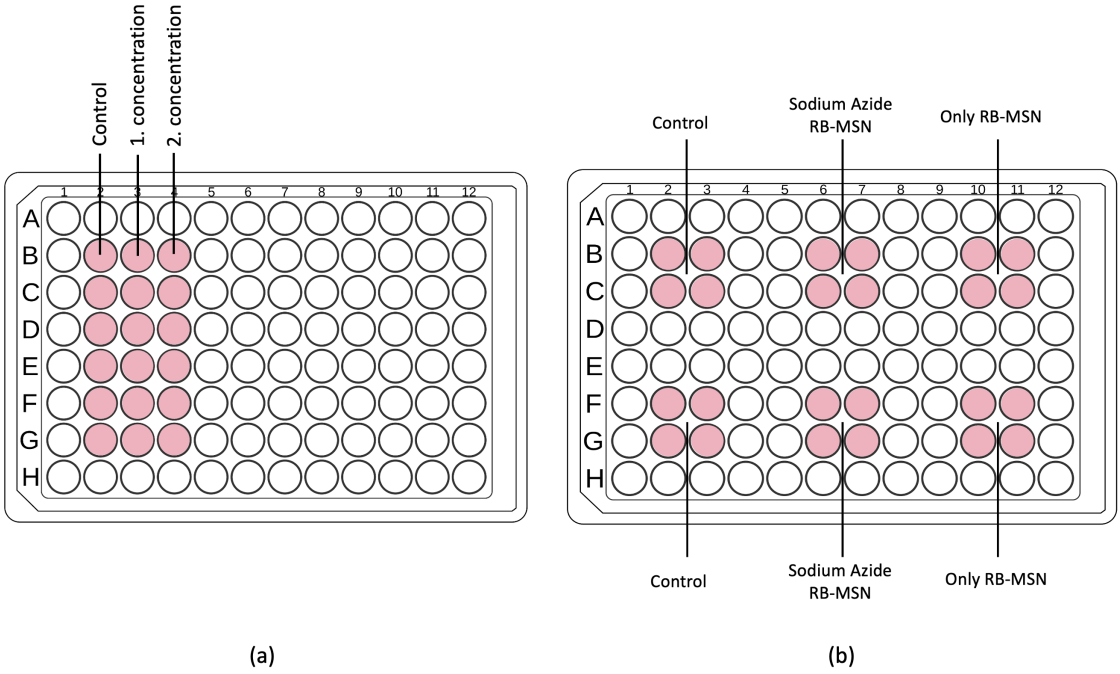

Figure 3.6 Illustration of the seeding layout for sodium azide experiments (a) toxicity evaluation of sodium azide (b) evaluation the role of $^1O_2$ in cellular toxicity.

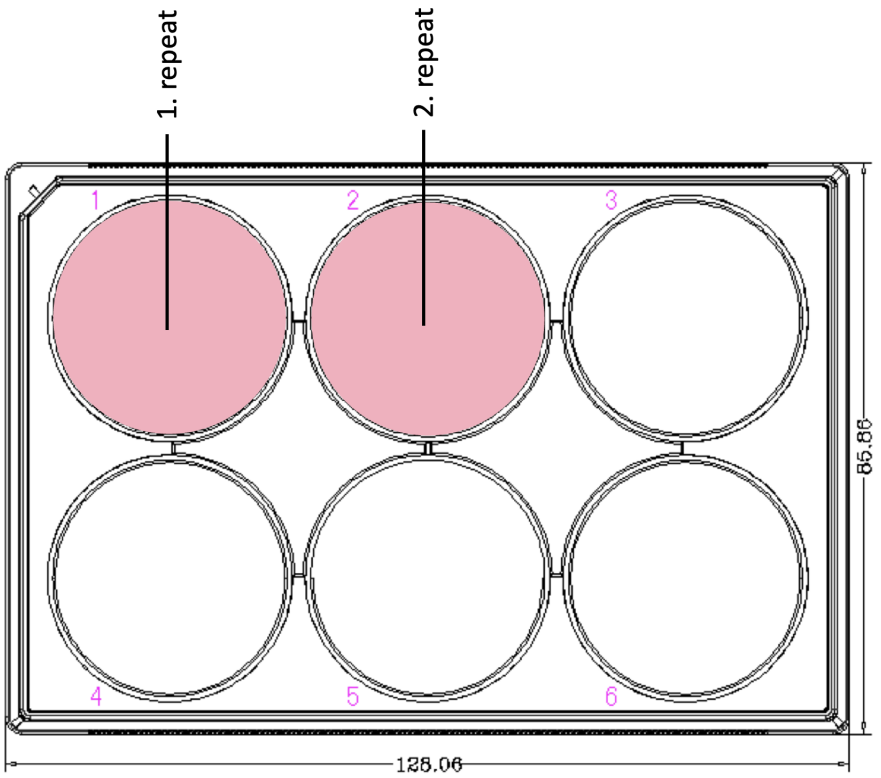

Figure 3.7 Illustration of the 6-well plate seeding layout for uptake experiments.

3.4 Configuration of laser equipment

RB has an absorption peak between 520 to 550 nm. For the light-based studies, we used a 530 nm LED light source (Thorlabs M530L4), as shown in the Figure 3.8. Prior to light application, each experiment's power density was set to 100 mW/cm^2. In PDT studies, different energy values were studied through changing the laser application time (1-min, 5-min, 10-min, 20-min). In the evaluation of $^1O_2$ capacity using sodium azide and quantification of $^1O_2$ production experiments were carried out by keeping the power density at 100 mW/cm^2.

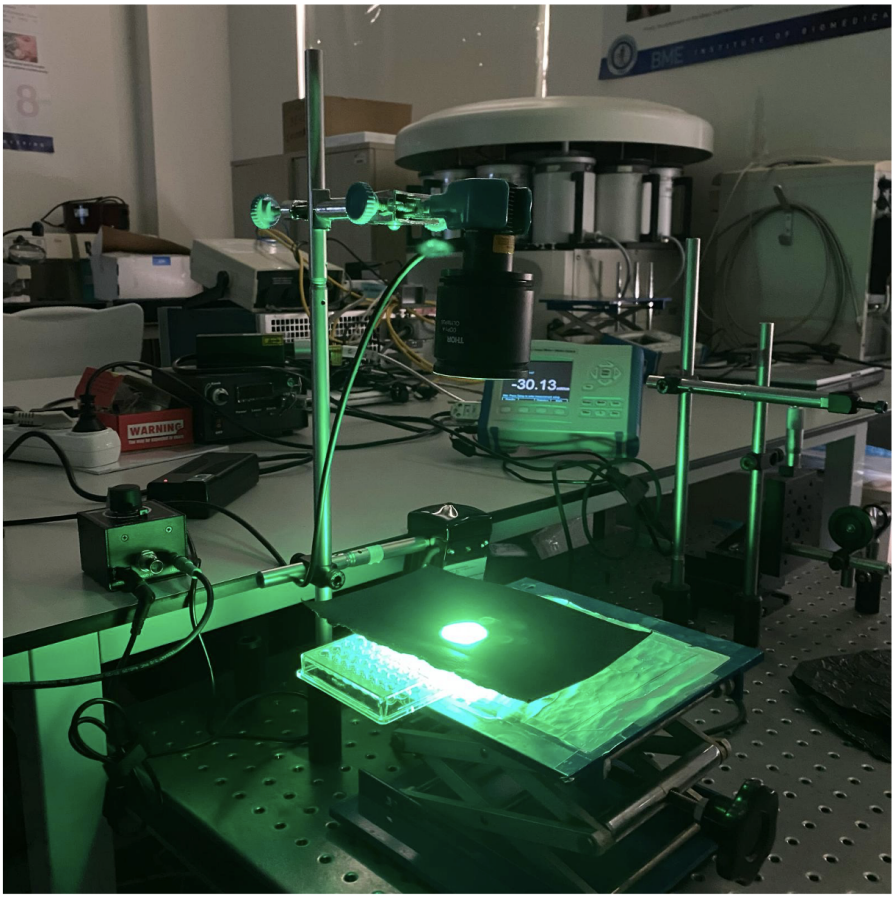

Figure 3.8 Experimentation setup for PDT. A light source with a wavelength of 530 nm used throughout the studies.

3.5 Dark toxicity experiments

Cells were seeded in incubated for 24 hours before being incubated with 5, 10, 25, 50, 100, 250, 500, 750, and 1000 µg/mL of RB-MSNs. After 2 hours of incubation, the RB-MSN-containing medium was refreshed. Plates were incubated for an additional 24 hours and MTT analysis performed.

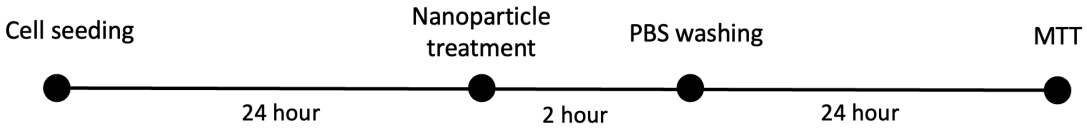

Figure 3.9 Experimental plan for dark-toxicity experiments.

3.5.1 Comparison of the dark toxicities of selected RB-MSNs concentrations with the dark toxicities of RB at the same concentration

Comparing RB-MSNs and RB at the same concentration is important to evaluate the toxicity of MSNs utilized as carriers.

After deciding on the concentration value to be used as a result of the dark toxicity experiments, the standard curve was first used to find the RB contained in RB-MSNs. The decided 750 µg/mL was added into 6 wells of the 96-well plate and the absorbtion value at 570 nm was measured. The absorbance value found corresponded to 49.25 µg/mL for RB.

Using the standard curve as a guide, control, RB-MSNs (750 µg/mL), and free RB (49.25 µg/mL) were added sequentially to the wells before incubating 2 hours. Plates were analyzed after MTT assay the following day.

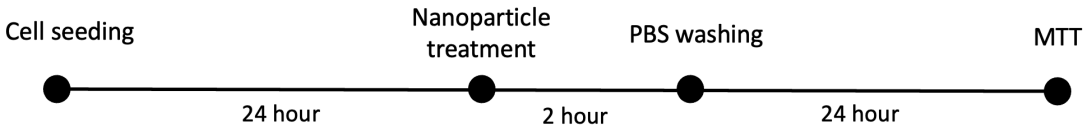

Figure 3.10 Experimental plan for comparing dark toxicities of RB-MSN and RB concentrations.

3.5.2 PDT experiments

For PDT experiments, cells were seeded into wells of 96-well plates. After 1 day incubation, RB-MSN solution at a concentration was applied. RB-MSNs were removed from the wells after 2-hours of incubation. Wells were washed before irradiation. A 530 nm LED light source (Thorlabs M530L4) was set to 100 mW/cm^2 to irradiate groups (except no light controls) for 1, 5, 10 and 20 minutes. After 24 hours of incubation, the MTT assay was applied.

Table 3.2
PDT parameters: irradiation periods, power density and corresponding energy doses.

Irradiation Period (minutes)	Power Density (mW/cm^2)	Energy Dose (J/cm^2)
1	100	6
5	100	30
10	100	60
20	100	120

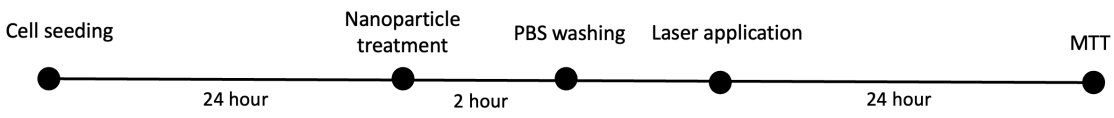

Figure 3.11 Experimental plan for PDT experiments.

3.5.3 Cellular uptake experiments

This experiment was conducted as described previously [50]. Briefly, the cells (1.5×10^5) were incubated for 24 hours. Concentrations of free RB and RB-MSNs were added to the wells at previously determined concentrations and incubated for 2 hours. After 2 hours of incubation, cells were detached from the surface using trypsin-EDTA. Cells were placed in 15 mL falcon tubes and counted. Subsequently, cells were centrifuged at 1000 rpm for 5 minutes and then gently washed with PBS. Each falcon tube was filled with 500 µL of a 90% acetone to extract RB from cells. Finally, the supernatants were transferred to a 96-well plate, and the absorption values were determined using an absorbance plate reader at 570 nm. The determined absorption values were compared with a previously sketched standard curve with the linear equation:

$$y = 0.0036x + 0.0962, \quad R^2 = 0.9979 \tag{3.1}$$

where x = supernatant average absorbance and y = supernatant molarity

The Eq. 3.2 is used to find RB contained in 1 µL of supernatant.

$$q = y \cdot \frac{M_{\text{rb}}}{10^6} \tag{3.2}$$

where q = RB quantity in 1 µL of supernatant and M_{rb} = molar weight of RB

Since the volume of the solution was 500 µL for each tube, the result was multiplied by 500. Finally, the amount of RB absorbed by a single cell was calculated by dividing the results for tubes by the corresponding number of cells. Two independent repeats were conducted.

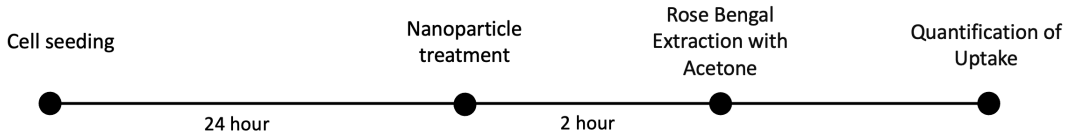

Figure 3.12 Experimental plan for cellular uptake experiments.

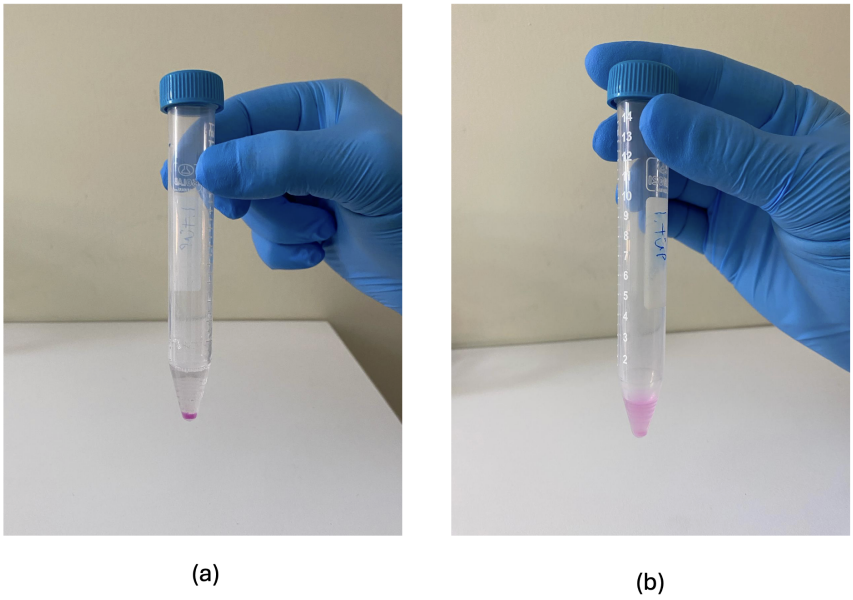

Figure 3.13 Falcon tubes (a) before and (b) after RB extraction.

3.5.4 Assessing the role of $^1O_2$ in cellular toxicity

Sodium azide is a $^1O_2$ quencher; therefore, it can be used to evaluate the dominant mechanism in PDT applications. In this analysis, inhibition of cell death when sodium azide presents in the medium would show that the cytotoxicity is mainly due to $^1O_2$ produced by Type II reactions during PDT [51],[52].

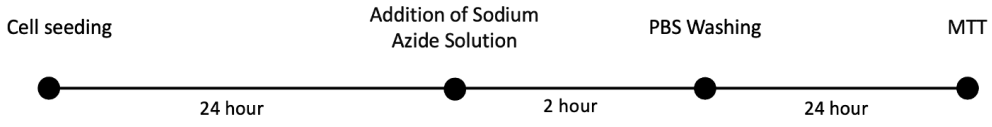

Figure 3.14 Experimental plan for toxicity evaluation experiments of sodium azide.

The reaction between sodium azide (NaN_3) and singlet oxygen $^1O_2$ is as follows:

$$NaN_3 + {}^1O_2 \longrightarrow N_3^- + O_2$$

First, a preliminary experiment was conducted to show that the sodium azide concentration that we use does not cause any toxicity on the A-549 cells. Briefly, cells were incubated with sodium azide (50 mM) for 2 hours and an MTT assay was performed. The cells were then plated and treated as follows:

- No treatment

- RB-MSNs and light (530 nm, 20 minutes, 100 mW/cm^2)

- RB-MSNs and light + sodium azide (530 nm, 20 minutes, 100 mW/cm^2).

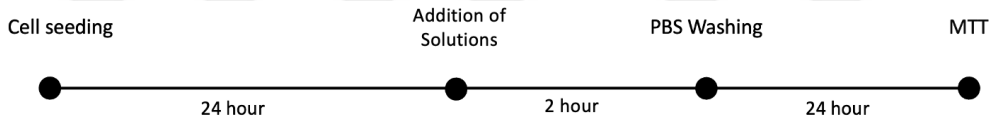

Figure 3.15 Experimental plan to evaluate the role of $^1O_2$ in cellular toxicity.

3.5.5 Quantification of ROS production using DPBF assay

RB and RB-MSNs were compared in terms of $^1O_2$ production using DPBF assay [53]. In this method, the PDT agents are incubated with DPBF and irradiated with light that can excite the PDT agents. The produced $^1O_2$ molecules during irradiation rapidly interact with DPBF, which causes a reduce in the absorbance peak of DPBF at 420 nm. Therefore, this decrease can be correlated with the $^1O_2$ production of the PDT agents. In our study, RB and RB-MSN concentrations that were previously determined by the dark toxicity experiments were separately incubated with 10 mM DPBF. The absorbance values following 0, 1, 5, 10 and 20 minutes of irradiation (530 nm, 100 mW/cm^2) were determined using the UV-Visible spectrophotometer at 420 nm. Two independent repeats were conducted.

3.5.6 Analysis of photodynamic stability

To compare the photostabilitiy of free RB and RB-MSNs, their previously determined concentrations were prepared in falcon tubes and kept at ambient temperature and light for 14 days. The absorption peaks of free RB and RB-MSNs at 550 nm were obtained and compared at 0, 3, 7, and 14 days.

3.5.7 Statistical analysis

The data was compared using student t-test (if two groups are compared) or ANOVA (if more than two groups are compared), after showing that the groups show a normal distribution. Tukey's multiple comparison test was performed to statistically compare the individual groups with each other. The significance level will be taken as 5% ($p<0.05$) and marked using a (*) symbol in the graphs. For all experiments, three independent repeats were conducted if otherwise specified.

4. RESULTS

4.1 Characterization of nanoparticles

The hydrodynamic diameters of MSNs were calculated as 60-70 nm (Figure 4.1). As shown in Figure 4.2, the synthesized MSNs reveal a uniform spherical morphology, and their sizes are similar to the results obtained from DLS. The results show that uniform MSNs could be successfully synthesized.

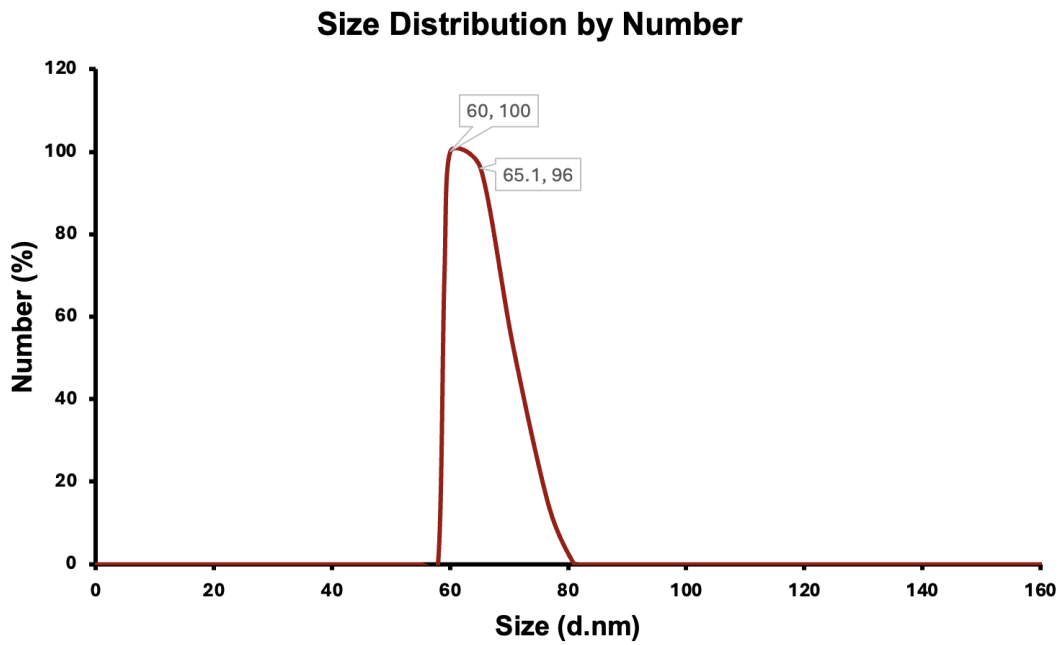

Figure 4.1 DLS measurements of MSNs.

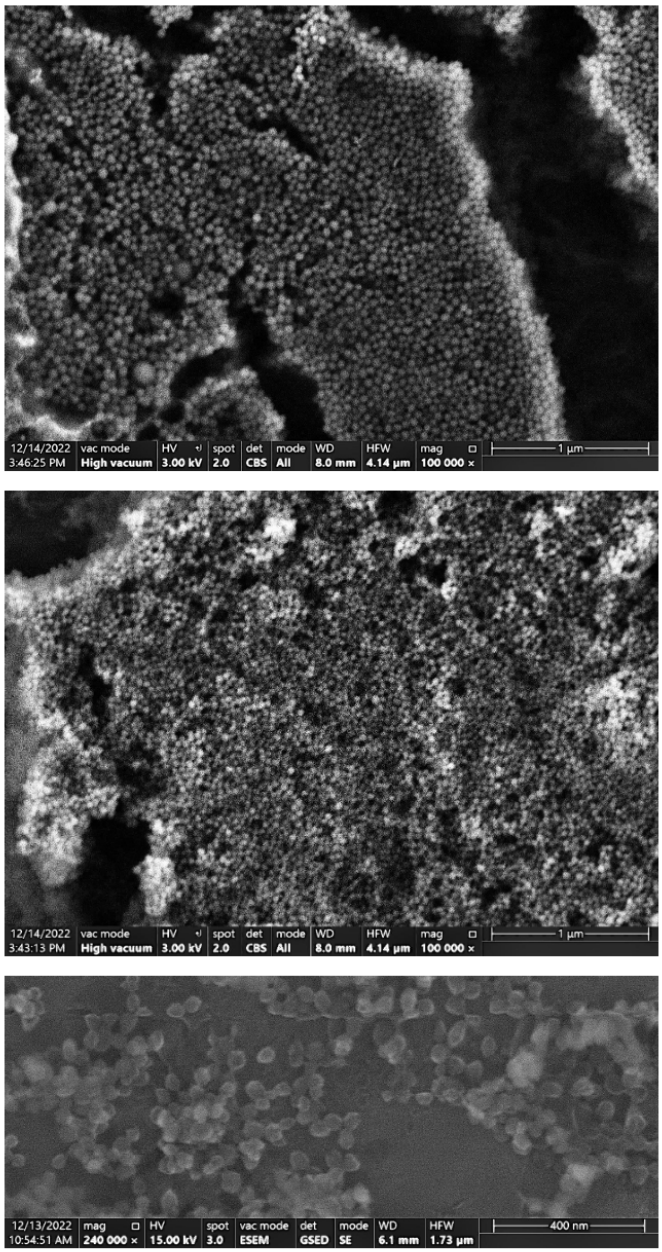

Figure 4.2 SEM images depicting the morphology and surface attributes of MSNs. Scale bars: 1 µm, 1 µm, and 400 nm for top, middle, and bottom images, respectively.

4.2 Dark toxicity experiments

As shown in Figure 4.3, RB-MSN was significantly toxic at 1000 µg/mL on A-549 cells. Therefore, the highest non-toxic concentration of RB-MSN, 750 µg/mL, was selected to be used in the following studies.

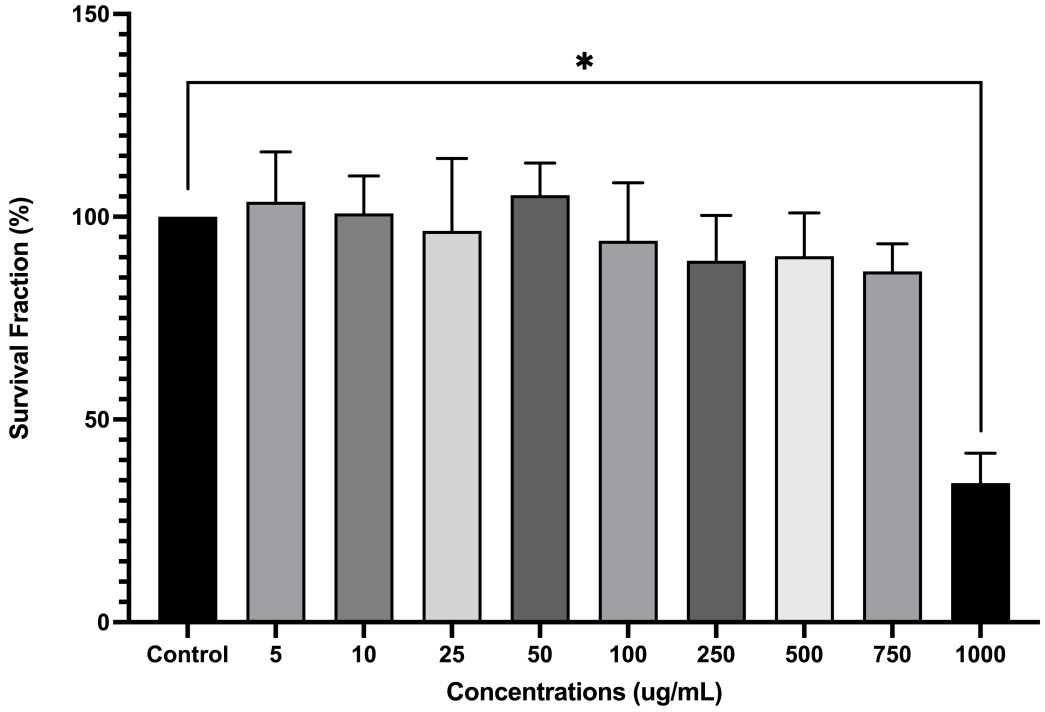

Figure 4.3 Survival fraction of A-549 cells with increasing RB-MSN concentration. Data of each group were normalized with respect the corresponding no treatment controls. Statistically significant group was labeled by " * " ($p < 0.05$).

4.3 Determination of RB content in RB-MSNs and calculation of encapsulation efficiency

The standard curve shown in Figure 4.4 was used to determine the RB amount in synthesized RB-MSNs. According to the linear equation derived from this curve (Figure 4.4), RB concentration in 750 µg/mL was calculated as 49.25 µg/mL. The comparison of the absorption spectra of these concentrations of free RB and RB-MSNs is shown in Figure 4.5. Similar absorption values confirm that the RB content of 750

µg/mL of RB-MSN is around 49.25 µg/mL.

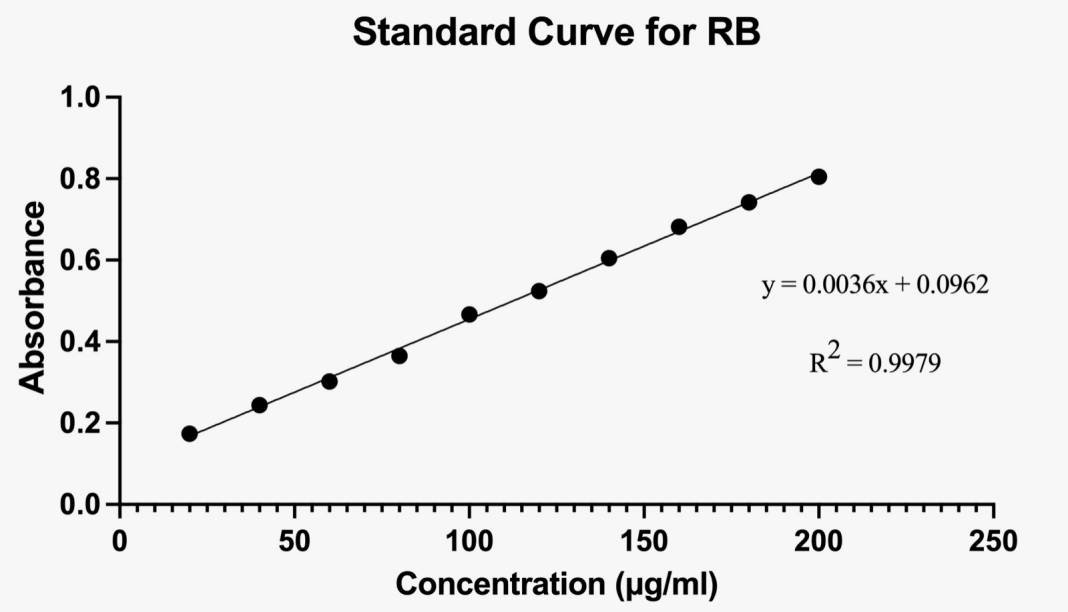

Figure 4.4 The standard curve for RB.

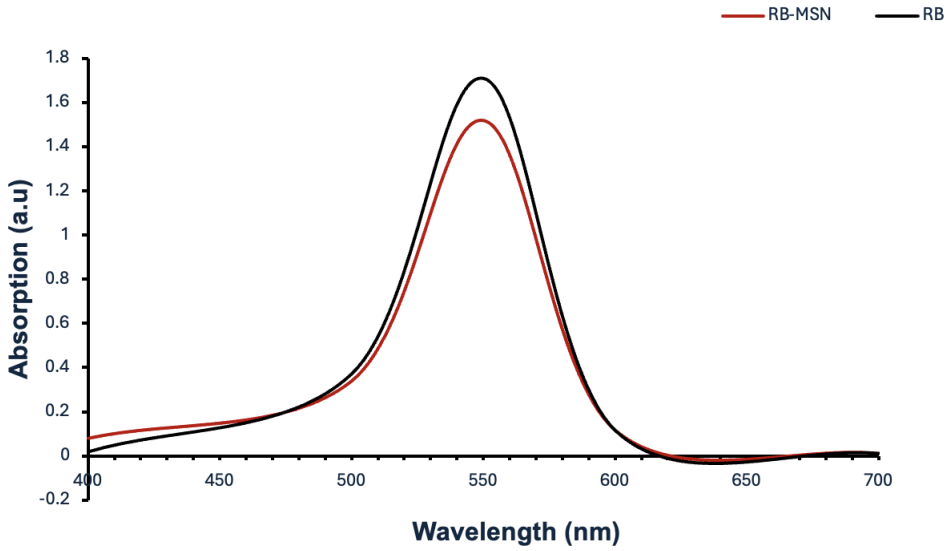

Figure 4.5 Absorbance spectrum of RB (49.25 µg/mL) and RB-MSN (750 µg /mL).

The encapsulation efficiency (EE) of RB within MSNs was determined using MPR and a calibration curve established for Rose Bengal. Based on the absorbance reading and the calibration curve:

$$C_{RB-MSN} = 49.25\,\mu\text{g/mL} = 0.04925\,\text{mg/mL}$$

where C_{RB-MSN} represents the concentration of Rose Bengal in the RB-MSN.

The mass of encapsulated Rose Bengal ($M_{encapsulated}$) can be calculated as follows:

$$M_{encapsulated} = C_{RB-MSN} \times V_{absorbance} \tag{4.1}$$

$$M_{encapsulated} = 0.04925\,\text{mg/mL} \times 6\,\text{mL}$$

$$M_{encapsulated} = 0.2955\,\text{mg}$$

The EE is determined by the ratio of the mass of encapsulated Rose Bengal to the total amount of Rose Bengal added:

$$\text{EE (\%)} = \left(\frac{M_{encapsulated}}{M_{RB}}\right) \times 100 \tag{4.2}$$

Substituting the given values:

$$\text{EE (\%)} = \left(\frac{0.2955\,\text{mg}}{3\,\text{mg}}\right) \times 100$$

$$\text{EE (\%)} = 9.85\%$$

4.4 Comparison of the dark toxicities of free RB and MSN-incorporated RB

As shown in Figure 4.6, RB (49.25 µg/mL) and RB-MSNs (750 µg/mL) did not show a significantly different toxicity to the survival fraction of A-549 cells compared to the no treatment control in the dark environment.

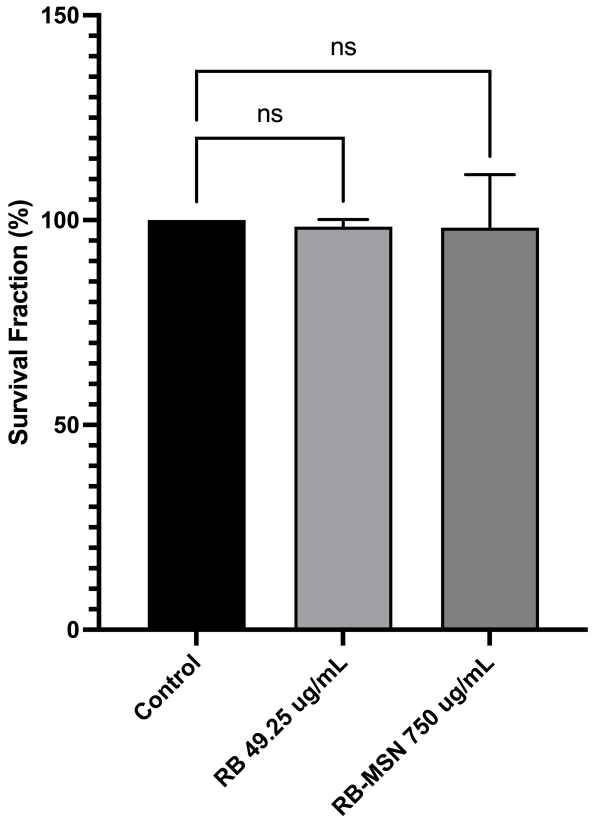

Figure 4.6 Survival fraction of A-549 cells incubated with RB (49.25 µg) and RB-MSNs (750 µg/mL). Data of each group were normalized with respect the corresponding no treatment controls. (ns: not significant).

4.5 PDT experiments

The results of the PDT experiment have shown that the application of light in the presence of RB-MSN caused a significant decrease in normalized survival of A-549 cells compared to the no treatment control groups (Figure 4.7). The highest reduction in cell survival, 72%, was achieved with 20 minutes of irradiation, although the groups that received light (PDT groups) did not show any significant difference.

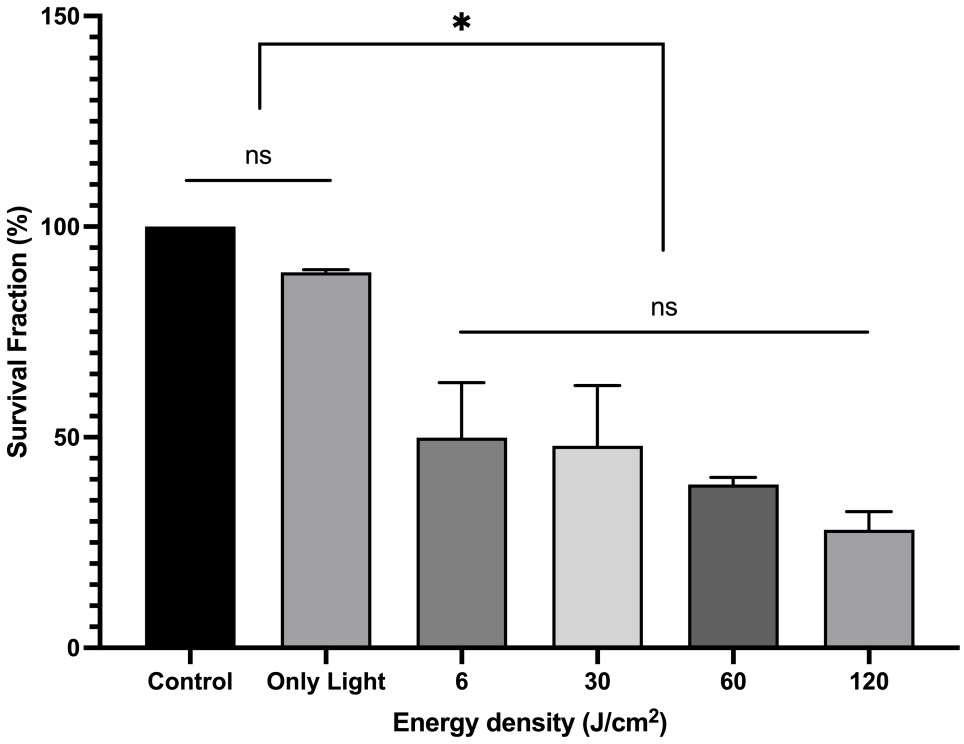

Figure 4.7 Survival fraction of A-549 cells incubated with RB-MSN and irradiated with given energy densities. Data of each group were normalized with respect to corresponding no treatment controls. Significant differences were labeled by " * " ($p < 0.05$).

4.6 Assessment of the primary mechanism of action of PDT

The results of the experiment show that 50 mM sodium azide does not cause any toxicity in cells (Figure 4.8). As shown in Figure 4.9, the results of the subsequent experiment showed that RB-MSNs-mediated PDT decreased the survival fraction by approximately 62% in the absence of sodium azide, whereas the same treatment could decrease the survival fraction by 13% in the presence of sodium azide. This shows that quenching $^1O_2$ using sodium azide significantly decreases the RB-MSNs-mediated PDT efficacy.

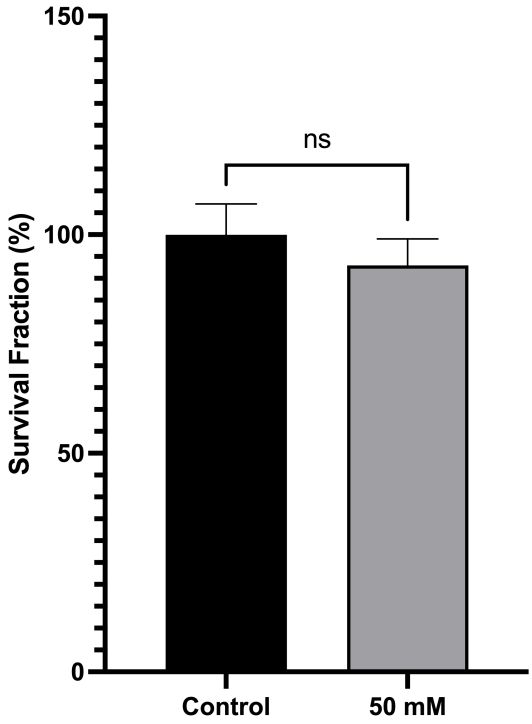

Figure 4.8 Assessment of dark toxicity with 50 mM sodium azide concentration in adherent A-549 cells using the MTT assay. (ns: not significant).

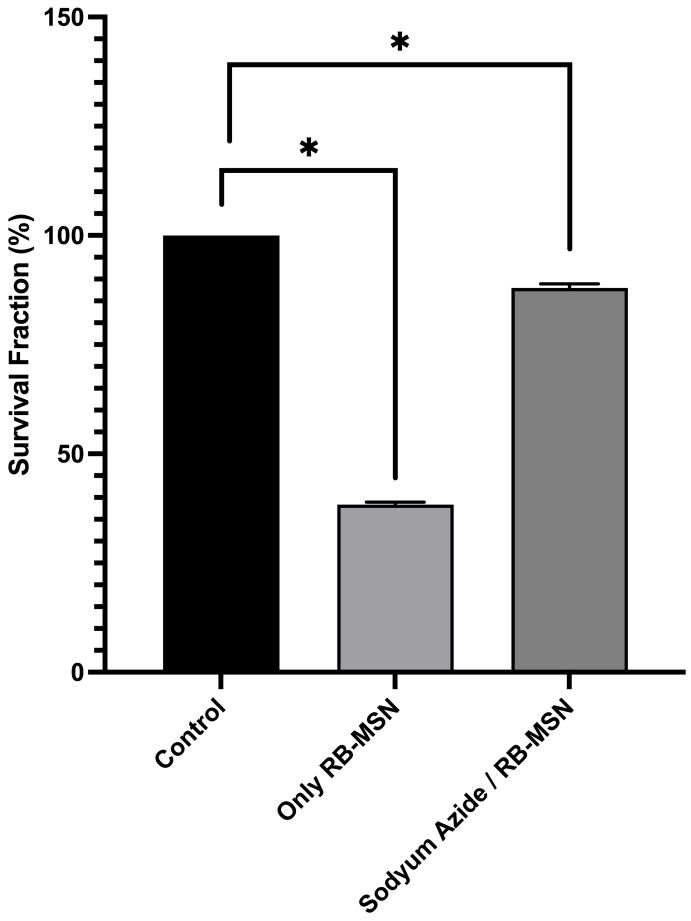

Figure 4.9 Survival fraction of A-549 cells after PDT when sodium azide absent or present in the medium. Data of each group were normalized with respect to corresponding no treatment controls. Significant groups are labeled by " * " ($p < 0.05$).

4.7 Singlet oxygen production for free and MSN-incorporated RB

DPBF assay was used to compare the $^1O_2$ production efficacy of free and MSN-incorporated RB. As shown in Figure 4.10 the $^1O_2$ production of MSN-incorporated RB was higher than free RB, which is consistent with the literature [41],[42].

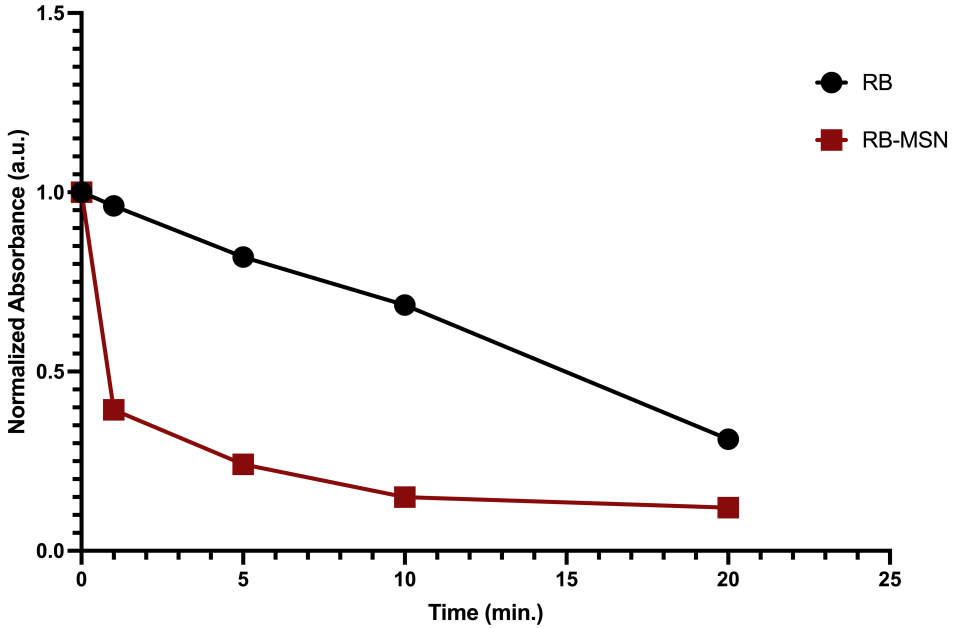

Figure 4.10 The change in absorption peak of DPBF after irradiation in the presence of RB (black/round) and RB-MSN (red/square).

4.8 Cellular uptake comparision of free and MSN-incorporated RB

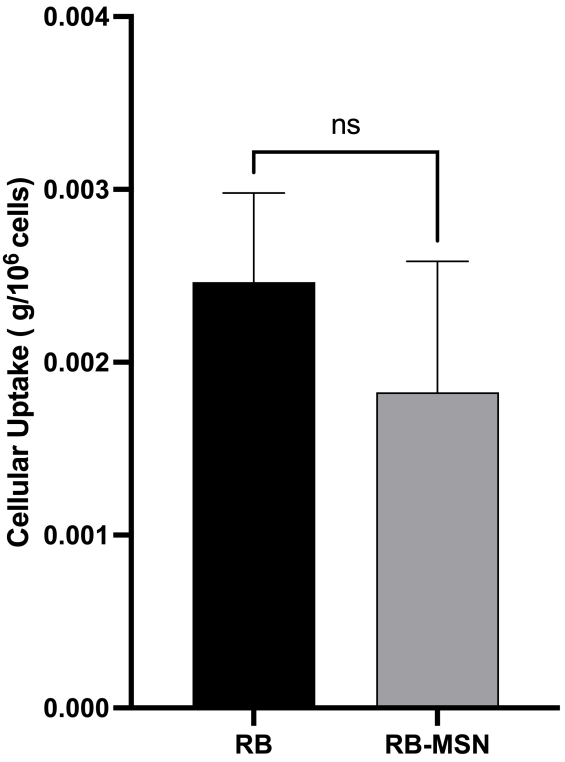

Figure 4.11 Comparison of cellular uptake of free RB and RB-MSN. ns: Not significant.

The graph shown in Figure 4.11 reveals that the cellular uptake of RB-MSNs was slightly less than free RB, although the difference was not statistically significantly different. This result suggests that the incorporation of RB molecules into MSN negatively affected their uptake by A-549 cells.

4.9 Comparison of the photostability of free and MSN incorporated RB

The curve shown in Figure 4.12(a) reveals that the absorbance of RB at 550 nm decreased continuously starting from the beginning of the experiment. The graph shown in Figure 4.12(c) of the same figure shows that this decrease is statistically significant between the 1st and 14th days of the experiment. On the other hand, the

absorbance of RB-incorporated MSNs at 550 nm did not significantly change (Figure 4.12(b).

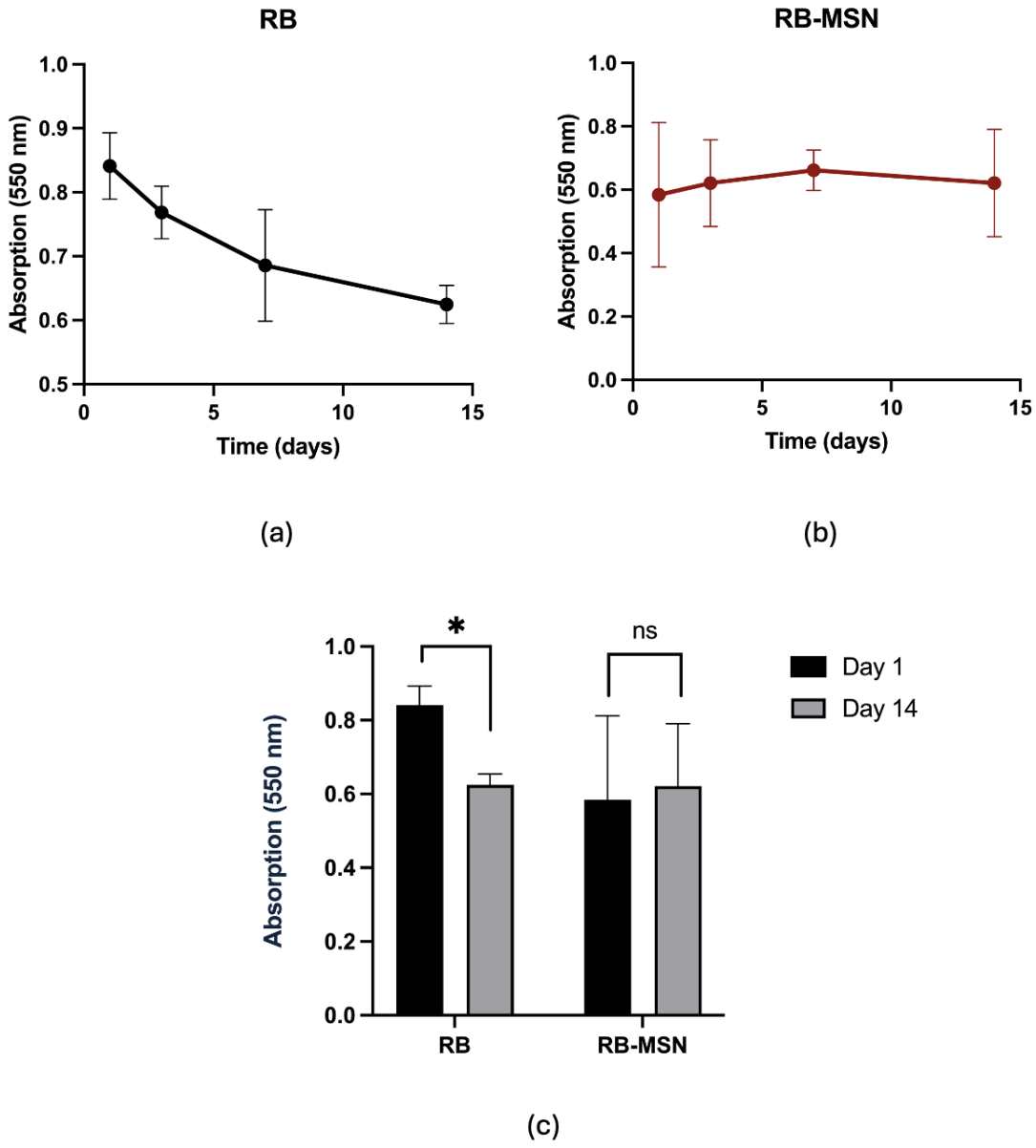

Figure 4.12 Photostability analysis results. a) Change in free RB absorbance at 550 nm. b) Change in RB-MSN absorbance at 550 nm. c) Comparison and statistical analysis of change in absorbance of RB (black/round) and RB-MSN (red/square) between Day 1 and Day 14. ns: Not significant.

5. DISCUSSIONS

The primary aim of this study was to evaluate the PDT efficacy of MSN-incorporated RB on an *in vitro* lung cancer model. High quantum yield of RB makes it an ideal candidate for generating $^1O_2$ in PDT. However, the 550 nm absorbance peak limits tissue penetration, consequently it is utilized primarily in superficial tumors like as breast, prostate, and ovarian cancer [54], [55]. However, advances in specialized light distribution systems and drug delivery approaches have renewed interest in RB for the treatment of deeper tumors [56]. Our work investigates the efficacy of RB-incorporated MSNs for lung cancer treatment, focusing on A-549 cells through toxicity, stability, oxygen generation, and cellular uptake assessments.

To characterize the nanoparticles, absorbance spectra of RB and RB-MSNs were measured. The maximum absorption value for both was at 550 nm, indicating effective encapsulation despite a slight decrease in RB-MSNs (Figure 4.5). Based on DLS results of mesoporous silica nanoparticles, the intensity plot peaks around 338 nm. A PDI of 0.238 confirms a fairly narrow size range, indicating uniformity among the nanoparticles (Figure 4.1). Under similar synthesis conditions, the sizes of MSNs were similar to the study by Catalano *et al.* [57] . SEM results revealed consistently spherical MSNs (Figure 4.2).

Dark toxicity studies of RB-MSNs at various concentrations showed no cytotoxic effect on A-549 cells up to 1000 µg/mL (Figure 4.3). The survival fraction decreased to 34% at this concentration. For PDT experiments, 750 µg/mL was selected to prevent side effects. Using the standard curve described in Section 4.3, the amount of RB in RB-MSNs was found to be 49.25 µg/mL. As shown in Figure 4.6, both RB and RB-MSNs exhibited no dark toxicity, with minimal reductions in cell survival (1.61% and 1.84%, respectively). PDT experiments demonstrated a significant reduction in survival fraction, validating the photodynamic efficacy of RB-MSNs (Figure 4.7). When cells treated with RB-MSNs (750 µg/mL) were exposed to various energy densities (6, 30,

60, and 120 (J/cm^2)), significant decrease in survival fraction was observed. Consistent with our results, in the study conducted by Yana *et al.*, RB and RB-MSNs did not show dark toxicity at concentrations similar to our study. When exposed to light, the survival rate of MCF-7 cells decreased significantly [58].

Sodium azide is a chemical that acts as a $^1O_2$ quencher. In the investigation the role of $^1O_2$ in cellular toxicity, Sodium Azide / RB-MSN and RB-MSN groups were compared after exposure to light. Figure 4.9 showed that the survival fraction of cells treated with RB-MSNs was significantly reduced compared to cells treated with Sodium azide / RB-MSNs. The results showed that the main mechanism of action of RB-mediated PDT remains dependent on $^1O_2$ production even after MSN was incorporated. However, there was a small decrease in the survival rate of cells treated with RB-MSNs in the presence of sodium azide. This result showed that the type 1 reaction also contributed to reduced survival rate, although not as much as the type 2 reaction. Additionally, $^1O_2$ production efficacy was evaluated using the DPBF assay. The results showed that RB-MSNs produced more $^1O_2$ than free RB (Figure 4.10). Paramananthama *et al.* evaluated the ROS-producing capacity of RB, MSNs and RB-MSNs. Consistent with our result, the authors showed that RB-MSNs have a higher ROS production capacity than RB and MSNs [59].

Cellular uptake comparision of free RB and RB-MSN is shown in Figure 4.11. The results revealed there was not significant difference in cellular uptake between RB and RB-MSN by A-549 cells. According to similar studies, we hypothesized that incorporation of hydrophilic RB into MSN would result in an increase in cellular uptake but the results did not show such an effect. In the study conducted by Zhan *et al.*, RB incorporated magnetic-MSNs showed higher cellular uptake by B-16 cells compared to free RB [45]. However, it should be kept in mind that these experiments were conducted on an *in vitro* model and the real effect of this drug delivery strategy would be revealed in *in vivo* conditions where circulation and extravasation take place.

There are studies in the literature showing that the incorporation of MSNs increase the photostability of PS [44],[48]. In our study, the stability of RB increased significantly when incorporated into MSNs (Figure 4.12). We believe that functionalization of MSNs with APTES improves the RB loading rate and increases nanoparticle stability. This surface modification method also prevented the aggregation of incorporated molecules within MSN pores, ensuring uniform dispersion. These modifications create a protective environment for RB, stabilizing its molecular structure and improving overall treatment efficacy.

Despite these promising findings, our study was conducted on the monolayer culture of one cancer cell line therefore, additional studies are necessary to reveal the effectiveness of RB-MSN as a PDT agent. Future research will focus on investigating the efficacy of this method on *in vivo* models and modifying the nanoparticles to further enhance the efficacy of the proposed treatment accordingly. Combining this method with traditional treatment approaches can also be explored to improve overall therapeutic outcomes.

To sum up, this study aimed to perform a comprehensive investigation of successfully synthesized RB-MSN nanoparticles in terms of photostability, cellular uptake, photochemical mechanism and PDT efficacy. The results revealed that the incorporation of RB with MSN enhanced its properties as a PDT agent.

6. CONCLUSIONS

In conclusion, our findings underline the potential of drug delivery system-based treatments to enhance cancer therapy effectiveness. This study evaluate the PDT efficacy of MSN incorporated RB on an *in vitro* lung cancer model. Results show that incorporating Rose Bengal into mesoporous silica increased its efficacy as a photodynamic therapy agent, overcoming the dye's limitations as a photosensitizer.

The incorporation of MSNs increased the $^1O_2$ production capacity of RB, probably due to the reduced degradation and increased local concentrations of RB molecules in MSN. Additionally, Rose Bengal's photostability was enhanced when incorporated into MSNs, although cellular uptake did not show a significant difference.

This study serves as a guide for MSN based drug delivery in PDT studies. Future research will investigate the effectiveness of this method on *in vivo* models and modify nanoparticle characteristics to increase the success of the proposed treatment. Combining this technique with conventional therapy approaches may also improve overall therapeutic outcomes.

REFERENCES

1. Torre, L. A., R. L. Siegel, and A. Jemal, "Lung cancer statistics," *Lung cancer and personalized medicine: current knowledge and therapies*, pp. 1–19, 2016.

2. Walter, F. M., G. Rubin, C. Bankhead, H. Morris, N. Hall, K. Mills, C. Dobson, R. Rintoul, W. Hamilton, and J. Emery, "Symptoms and other factors associated with time to diagnosis and stage of lung cancer: a prospective cohort study," *British Journal of Cancer*, Vol. 112, no. 1, pp. S6–S13, 2015.

3. Chilakamarthi, U., and L. Giribabu, "Photodynamic therapy: past, present and future," *The Chemical Record*, Vol. 17, no. 8, pp. 775–802, 2017.

4. Pinto da Silva, L., C. M. Magalhães, A. Nunez-Montenegro, P. J. Ferreira, D. Duarte, J. E. Rodríguez-Borges, N. Vale, and J. C. Esteves da Silva, "Study of the combination of self-activating photodynamic therapy and chemotherapy for cancer treatment," *Biomolecules*, Vol. 9, no. 8, p. 384, 2019.

5. Gunaydin, G., M. E. Gedik, and S. Ayan, "Photodynamic therapy current limitations and novel approaches," *Frontiers in Chemistry*, Vol. 9, p. 691697, 2021.

6. Lucky, S. S., K. C. Soo, and Y. Zhang, "Nanoparticles in photodynamic therapy," *Chemical Reviews*, Vol. 115, no. 4, pp. 1990–2042, 2015.

7. Zhen, Z., W. Tang, Y.-J. Chuang, T. Todd, W. Zhang, X. Lin, G. Niu, G. Liu, L. Wang, Z. Pan, *et al.*, "Tumor vasculature targeted photodynamic therapy for enhanced delivery of nanoparticles," *ACS Nano*, Vol. 8, no. 6, pp. 6004–6013, 2014.

8. Luo, X., B. Zhang, Y. Zhang, Z. Meng, P. Li, X. Jiang, C. Lin, W. Su, *et al.*, "Rose bengal-modified gold nanorods for ptt/pdt antibacterial synergistic therapy," *Photodiagnosis and Photodynamic Therapy*, Vol. 39, p. 102988, 2022.

9. Fadel, M., and K. Kassab, "Evaluation of the photostability and photodynamic efficacy of rose bengal loaded in multivesicular liposomes," *Tropical Journal of Pharmaceutical Research*, Vol. 10, no. 3, 2011.

10. Lan, M., S. Zhao, W. Liu, C.-S. Lee, W. Zhang, and P. Wang, "Photosensitizers for photodynamic therapy," *Advanced Healthcare Materials*, Vol. 8, no. 13, p. 1900132, 2019.

11. Filonenko, E., and L. Serova, "Photodynamic therapy in clinical practice," *Biomedical Photonics*, Vol. 5, no. 2, pp. 26–37, 2016.

12. Chu, B., Y. Qu, X. He, Y. Hao, C. Yang, Y. Yang, D. Hu, F. Wang, and Z. Qian, "Ros-responsive camptothecin prodrug nanoparticles for on-demand drug release and combination of chemotherapy and photodynamic therapy," *Advanced Functional Materials*, Vol. 30, no. 52, p. 2005918, 2020.

13. Ferlay, J., M. Colombet, I. Soerjomataram, D. M. Parkin, M. Piñeros, A. Znaor, and F. Bray, "Cancer statistics for the year 2020: An overview," *International Journal of Cancer*, Vol. 149, no. 4, pp. 778–789, 2021.

14. Sharma, R., "Mapping of global, regional and national incidence, mortality and mortality-to-incidence ratio of lung cancer in 2020 and 2050," *International Journal of Clinical Oncology*, Vol. 27, no. 4, pp. 665–675, 2022.

15. Torre, L. A., R. L. Siegel, E. M. Ward, and A. Jemal, "Global cancer incidence and mortality rates and trendsâan update," *Cancer Epidemiology, Biomarkers & Prevention*, Vol. 25, no. 1, pp. 16–27, 2016.

16. Oser, M. G., M. J. Niederst, L. V. Sequist, and J. A. Engelman, "Transformation from non-small-cell lung cancer to small-cell lung cancer: molecular drivers and cells of origin," *The Lancet Oncology*, Vol. 16, no. 4, pp. e165–e172, 2015.

17. Pelosi, G., M. Barbareschi, A. Cavazza, P. Graziano, G. Rossi, and M. Papotti, "Large cell carcinoma of the lung: a tumor in search of an author. a clinically oriented critical reappraisal," *Lung Cancer*, Vol. 87, no. 3, pp. 226–231, 2015.

18. De Stefani, E., P. Boffetta, A. L. Ronco, P. Brennan, P. Correa, H. Deneo-Pellegrini, L. P. Gutiérrez, and M. Mendilaharsu, "Squamous and small cell carcinomas of the lung: similarities and differences concerning the role of tobacco smoking," *Lung Cancer*, Vol. 47, no. 1, pp. 1–8, 2005.

19. Sudhakar, A., "History of cancer, ancient and modern treatment methods," *Journal of Cancer Science & Therapy*, Vol. 1, no. 2, p. 1, 2009.

20. Castano, A. P., T. N. Demidova, and M. R. Hamblin, "Mechanisms in photodynamic therapy: part oneâphotosensitizers, photochemistry and cellular localization," *Photodiagnosis and Photodynamic Therapy*, Vol. 1, no. 4, pp. 279–293, 2004.

21. Kübler, A. C., "Photodynamic therapy," *Medical Laser Application*, Vol. 20, no. 1, pp. 37–45, 2005.

22. Niculescu, A.-G., and A. M. Grumezescu, "Photodynamic therapyâan up-to-date review," *Applied Sciences*, Vol. 11, no. 8, p. 3626, 2021.

23. Zhang, Q., and L. Li, "Photodynamic combinational therapy in cancer treatment," *J. BUON*, Vol. 23, no. 3, pp. 561–567, 2018.

24. Brodin, N. P., C. Guha, and W. A. Tomé, "Photodynamic therapy and its role in combined modality anticancer treatment," *Technology in Cancer Research & Treatment*, Vol. 14, no. 4, pp. 355–368, 2015.

25. Brown, S. B., E. A. Brown, and I. Walker, "The present and future role of photodynamic therapy in cancer treatment," *The Lancet Oncology*, Vol. 5, no. 8, pp. 497–508, 2004.

26. Sharma, S. K., P. Mroz, T. Dai, Y.-Y. Huang, T. G. S. Denis, and M. R. Hamblin, "Photodynamic therapy for cancer and for infections: what is the difference?," *Israel Journal of Chemistry*, Vol. 52, no. 8-9, pp. 691–705, 2012.

27. Dąbrowski, J. M., "Reactive oxygen species in photodynamic therapy: mechanisms of their generation and potentiation," in *Advances in Inorganic Chemistry*, Vol. 70, pp. 343–394, Elsevier, 2017.

28. Maharjan, P. S., H. K. Bhattarai, *et al.*, "Singlet oxygen, photodynamic therapy, and mechanisms of cancer cell death," *Journal of Oncology*, Vol. 2022, 2022.

29. Jain, K. K., "Current status and future prospects of drug delivery systems," *Drug Delivery System*, pp. 1–56, 2014.

30. Cho, K., X. Wang, S. Nie, Z. Chen, and D. M. Shin, "Therapeutic nanoparticles for drug delivery in cancer," *Clinical Cancer Research*, Vol. 14, no. 5, pp. 1310–1316, 2008.

31. Maeda, H., "The enhanced permeability and retention (epr) effect in tumor vasculature: the key role of tumor-selective macromolecular drug targeting," *Advances in Enzyme Regulation*, Vol. 41, no. 1, pp. 189–207, 2001.

32. Allen, T. M., and P. R. Cullis, "Liposomal drug delivery systems: from concept to clinical applications," *Advanced Drug Delivery Reviews*, Vol. 65, no. 1, pp. 36–48, 2013.

33. Shi, J., A. R. Votruba, O. C. Farokhzad, and R. Langer, "Nanotechnology in drug delivery and tissue engineering: from discovery to applications," *Nano Letters*, Vol. 10, no. 9, pp. 3223–3230, 2010.

34. Allahou, L. W., S. Y. Madani, A. Seifalian, *et al.*, "Investigating the application of liposomes as drug delivery systems for the diagnosis and treatment of cancer," *International Journal of Biomaterials*, Vol. 2021, 2021.

35. Chan, J. M., P. M. Valencia, L. Zhang, R. Langer, and O. C. Farokhzad, "Polymeric nanoparticles for drug delivery," *Cancer Nanotechnology: Methods and Protocols*, pp. 163–175, 2010.

36. Tomalia, D. A., "Dendrimers as multi-purpose nanodevices for oncology drug delivery and diagnostic imaging," *Nanomedicine: Nanotechnology, Biology, and Medicine*, Vol. 4, no. 2, p. 309, 2006.

37. Hussein, Y. H., and M. Youssry, "Polymeric micelles of biodegradable diblock copolymers: enhanced encapsulation of hydrophobic drugs," *Materials*, Vol. 11, no. 5, p. 688, 2018.

38. Liang, R., M. Wei, D. G. Evans, and X. Duan, "Inorganic nanomaterials for bioimaging, targeted drug delivery and therapeutics," *Chemical Communications*, Vol. 50, no. 91, pp. 14071–14081, 2014.

39. Hossen, S., M. K. Hossain, M. Basher, M. Mia, M. Rahman, and M. J. Uddin, "Smart nanocarrier-based drug delivery systems for cancer therapy and toxicity studies: A review," *Journal of Advanced Research*, Vol. 15, pp. 1–18, 2019.

40. Sztandera, K., M. Gorzkiewicz, and B. Klajnert-Maculewicz, "Nanocarriers in photodynamic therapyâin vitro and in vivo studies," *Wiley Interdisciplinary Reviews: Nanomedicine and Nanobiotechnology*, Vol. 12, no. 3, p. e1509, 2020.

41. Singh, A. K., M. A. Hahn, L. G. Gutwein, M. C. Rule, J. A. Knapik, B. M. Moudgil, S. R. Grobmyer, and S. C. Brown, "Multi-dye theranostic nanoparticle platform for bioimaging and cancer therapy," *International Journal of Nanomedicine*, pp. 2739–2750, 2012.

42. Mendoza, C., A. Désert, L. Khrouz, C. A. Páez, S. Parola, and B. Heinrichs, "Heterogeneous singlet oxygen generation: in-operando visible light epr spectroscopy," *Environmental Science and Pollution Research*, Vol. 28, pp. 25124–25129, 2021.

43. Estevão, B. M., F. Cucinotta, N. Hioka, M. Cossi, M. Argeri, G. Paul, L. Marchese, and E. Gianotti, "Rose bengal incorporated in mesostructured silica nanoparticles: structural characterization, theoretical modeling and singlet oxygen delivery," *Physical Chemistry Chemical Physics*, Vol. 17, no. 40, pp. 26804–26812, 2015.

44. Gianotti, E., B. Martins Estevão, F. Cucinotta, N. Hioka, M. Rizzi, F. Renò, and L. Marchese, "An efficient rose bengal based nanoplatform for photodynamic therapy," *Chemistry–A European Journal*, Vol. 20, no. 35, pp. 10921–10925, 2014.

45. Zhan, J., Z. Ma, D. Wang, X. Li, X. Li, L. Le, A. Kang, P. Hu, L. She, and F. Yang, "Magnetic and ph dual-responsive mesoporous silica nanocomposites for effective and low-toxic photodynamic therapy," *International Journal of Nanomedicine*, pp. 2733–2748, 2017.

46. Lin, Y.-S., and C. L. Haynes, "Impacts of mesoporous silica nanoparticle size, pore ordering, and pore integrity on hemolytic activity," *Journal of the American Chemical Society*, Vol. 132, no. 13, pp. 4834–4842, 2010.

47. Ahmadi, E., N. Dehghannejad, S. Hashemikia, M. Ghasemnejad, and H. Tabebordbar, "Synthesis and surface modification of mesoporous silica nanoparticles and its application as carriers for sustained drug delivery," *Drug Delivery*, Vol. 21, no. 3, pp. 164–172, 2014.

48. Wang, Y., Y. Sun, J. Wang, Y. Yang, Y. Li, Y. Yuan, and C. Liu, "Charge-reversal aptes-modified mesoporous silica nanoparticles with high drug loading and release controllability," *ACS Applied Materials & Interfaces*, Vol. 8, no. 27, pp. 17166–17175, 2016.

49. Goldburg, W. I., "Dynamic light scattering," *American Journal of Physics*, Vol. 67, no. 12, pp. 1152–1160, 1999.

50. Colasanti, A., A. Kisslinger, M. Quarto, and P. Riccio, "Combined effects of radiotherapy and photodynamic therapy on an in vitro human prostate model.," *Acta Biochimica Polonica*, Vol. 51, no. 4, pp. 1039–1046, 2004.

51. Tavares, A., S. R. Dias, C. M. Carvalho, M. A. Faustino, J. P. Tome, M. G. Neves, A. C. Tome, J. A. Cavaleiro, A. Cunha, N. C. Gomes, *et al.*, "Mechanisms of photodynamic inactivation of a gram-negative recombinant bioluminescent bacterium by cationic porphyrins," *Photochemical & Photobiological Sciences*, Vol. 10, no. 10, pp. 1659–1669, 2011.

52. Hamblin, M. R., "Potentiation of antimicrobial photodynamic inactivation by inorganic salts," *Expert Review of Anti-infective Therapy*, Vol. 15, no. 11, pp. 1059–1069, 2017.

53. Entradas, T., S. Waldron, and M. Volk, "The detection sensitivity of commonly used singlet oxygen probes in aqueous environments," *Journal of Photochemistry and Photobiology B: Biology*, Vol. 204, p. 111787, 2020.

54. Koevary, S. B., "Selective toxicity of rose bengal to ovarian cancer cells in vitro," *International Journal of Physiology, Pathophysiology and Pharmacology*, Vol. 4, no. 2, p. 99, 2012.

55. Uddin, M. M. N., A. Bekmukhametova, A. Antony, S. K. Barman, J. Houang, M. J. Wu, J. Hook, L. George, R. Wuhrer, D. Mawad, *et al.*, "Photodynamic treatment of human breast and prostate cancer cells using rose bengal-encapsulated nanoparticles," *Molecules*, Vol. 28, no. 19, p. 6901, 2023.

56. Algorri, J. F., M. Ochoa, P. Roldan-Varona, L. Rodriguez-Cobo, and J. M. López-Higuera, "Light technology for efficient and effective photodynamic therapy: A critical review," *Cancers*, Vol. 13, no. 14, p. 3484, 2021.

57. Catalano, F., and P. P. Pompa, "Design rules for mesoporous silica toward the nanosize: a systematic study," *ACS Applied Materials & Interfaces*, Vol. 11, no. 50, pp. 47237–47246, 2019.

58. Yan, T., J. Cheng, Z. Liu, F. Cheng, X. Wei, and J. He, "ph-sensitive mesoporous silica nanoparticles for chemo-photodynamic combination therapy," *Colloids and Surfaces B: Biointerfaces*, Vol. 161, pp. 442–448, 2018.

59. Paramanantham, P., A. P. Antony, S. S. Lal, A. Sharan, A. Syed, M. Ahmed, A. A. Alarfaj, S. Busi, M. Maaza, and K. Kaviyarasu, "Antimicrobial photodynamic inactivation of fungal biofilm using amino functionalized mesoporus silica-rose bengal nanoconjugate against candida albicans," *Scientific African*, Vol. 1, p. e00007, 2018.